KU LEUVEN

FACULTY OF SCIENCES

Broadband laser spectroscopy of RaF

Carlos Mario Fajardo Zambrano

CERN-THESIS-2023-239
06/06/2023

Supervisor: Prof. G. Neyens
Institute for Nuclear and Radiation Physics (KU Leuven)

Tutors: M. Athanasakis-Kaklamanakis & B. van den Borne
Institute for Nuclear and Radiation Physics (KU Leuven)

Master thesis submitted in fulfillment of the requirements for the degree in Master of Science in Physics

Academic year 2022-2023

Acknowledgements

It's funny to think that two years have already passed since I started my master, being the present work the last step in this journey. Since this work has only been possible with the help of many wonderful people, I feel obliged to dedicate a couple of words to them.

First, I would like to thank my supervisor Prof. Gerda Neyens, for her continuous support and guidance and for allowing me to work in this emerging field. I would like to thank Michail for his continuous help and advice, to the point that being in different countries never felt like a limitation, and for providing me with all the bases necessary to tackle my thesis. Similarly, I'm grateful to Bram for his knowledge of data analysis and good beers and for being my tutor from the beginning, even without knowing.

I would like to thank all the different members of the CRIS collaboration for providing me with the data on which this work has been based, as well as helping me out on different occasions every time I end up having a random question.

I'm also grateful to my master's classmates, PhD colleagues, post-Doc, and professors for providing me with your help and whose contribution might not be stress-out in this work but genuinely made part to its conclusion.

Finalmente, pero no menos importante, quisiera darle las gracias a mis padres y hermana, por ser mi mayor soporte, siempre creer en mí y ser quienes me han permitido alcanzar todos mis logros.

Scientific summary

With the advancement of spectroscopic techniques at radioactive beam facilities, the spectroscopy of radioactive molecules has been achieved in the past few years at ISOLDE (CERN) using the Collinear Resonance Ionization Spectroscopy (CRIS) experiment.

The study of radioactive molecules is an emerging and promising discovery tool for diverse fields. Among them, diatomic polar molecules are at the center of theoretical and experimental investigations in search of the electron's electric dipole moment (eEDM) and nuclear Schiff moments. Due to the strong electric field and the rich electronic, vibrational, and rotational structure inherent in molecules, the sensitivity to Schiff moments is expected to be enhanced in radioactive polar molecules, such as RaF. However, their molecular structure is poorly known, requiring preparatory spectroscopic studies of the electronic structure of the molecule.

After two experimental campaigns at CRIS (2018, 2021), many electronic levels in RaF have been studied with broadband laser spectroscopy, as well as one optical transition in high resolution. This has shown the capacity of collinear laser spectroscopy at radioactive ion beam facilities for the study of radioactive molecules, as well as benchmarking the predictive power of state-of-the-art quantum chemistry.

The present work focus on the analysis and retrieval of the molecular constant of the different electronic levels measured in the 2021 RaF campaign. To do so, PGOPHER has been implemented to simulate and fit the experimental spectrum retrieved. Furthermore, the influence of the population distribution in the measurement of the low-lying electronic states has also been studied, exhibiting a non-uniform cooling of the molecules arriving at CRIS.

Summary for general audience

One of the main problems of fundamental physics is the well-known CP problem. In essence, this is the conservation of two different symmetries at the same time. Similar to the symmetry between a person and his reflection in a mirror. This problem is relevant as different unsolved problems in physics could be explained if this double symmetry can be breakable. However, so far, it has not been measured experimentally.

One of the most promising attempts nowadays is its indirect measurement in diatomic molecules with specific conditions, such as being made by a super-heavy atom. Unfortunately, most of the atoms that could be used for these studies are radioactive, i.e., they decay with time until they are converted into another one, hindering our capacity to perform measurements on them. Nevertheless, the first short-live molecule, Radium fluoride (RaF), has already been measured in 2018 at ISOLDE, a facility in CERN, Geneva, focused on the production of radioactive beams.

The detection of this breakable symmetry is based on the measurement of a small displacement in the nominal value of an inherit property of the molecule (the molecular energy levels). However, to determine this displacement, these energy levels of RaF have to be well known. As such, the current work is a preliminary study focused on the different variables that define the energy levels of RaF, as well as the considerations needed for its retrieval. Based on the experimental data retrieved, most of the energy levels of RaF have been successfully measured and show an extremely high accuracy when compared with the theoretical predictions. However, further studies with higher precision are needed to experimentally verify the CP problem.

List of Figures

List of Tables

Contents

Chapter 1

Introduction

One of the most frequent tools in electromagnetism is the multipolar decomposition of a charge-current distribution. This allows a complete description of the electromagnetic fields produced by the source and the coupling of external fields onto it (Alaee et al., 2018). Since the odd terms of the electric multipole expansion can only be present under parity and time-reversal violation (due to P, T-odd interactions) (Singh et al., 2013), and the higher moments are negligible, the electric multipole expansion is usually expressed in terms of the electric monopole and quadrupole moments. As such, the presence of a permanent electric dipole moment (EDM) in any physical system would be an indication of time-reversal (T) and parity (P) violation in the system (Purcell and Ramsey, 1950).

Due to the CPT conservation theorem (Greaves and Thomas, 2014), a T-violation implies the simultaneous violation of the invariance concerning charge conjugation (C) and spatial inversion (P). Despite that the CP violation has been measured in neutral K and B mesons, the limits on new physics have yet not been set (Ginges and Flambaum, 2004). As such, several studies of CP violation have been performed in the past decades as different theories, such as the supersymmetry and the universe matter-antimatter asymmetry (baryogenesis problem), can be explained through an unknown CP-violating interaction (Pospelov and Ritz, 2005; Flambaum and Dzuba, 2020). Such studies are typically in the realm of high-energy accelerator facilities such as the Large Hadron Collider (LHC) at CERN.

The study of the existence of an EDM in table-top high precision measurements is a current alternative to search for physics beyond the standard model as accelerator experiments become increasingly costly (Rossi and Brüning, 2012). However, both the Standard Model and various beyond Standard Model (BSM) theories predict extremely small values for the EDM (10^{-38} e.cm). Thus, probes that are highly sensitive to an EDM need to be identified, and experimental set-ups that allow for high-precision studies have to be devised.

In the past decades, atomic physics has played a major role in the search for possible physics beyond the standard model, including CP violation studies. An atomic EDM can be induced due to an inherited EDM of their constituents or due to P, T-odd interactions between them (Ginges and Flambaum, 2004). The latter can induce nuclear moments that polarize the atom and produces an atomic EDM directed along the nuclear spin (Flambaum and Dzuba, 2020). Among them, the Schiff moment, a vector moment representing the nuclei's electric field after considering the EDM screening by electrons, has appeared as the main contribution for close shell atoms due to P, T-odd interactions between nucleons.

Enhanced sensitivity to P, T-odd interactions is present in deformed nuclei with high nuclear charge (Z), collective behavior, and close levels of opposite parity. However, the major

enhancement happens in octupole-deformed nuclei, where the opposite parity and collective effect work together. According to Auerbach et al. (1996); Spevak et al. (1997), this happens in some isotopes of Fr, Rn, Ra, and actinide atoms, making them the most promising candidates for CP-violation studies. Unfortunately, all of these elements have only radioactive isotopes, no stable ones.

Currently, ^{199}Hg is the nucleus with the current best limit EDM, namely $S_{Hg} < 3 \times 10^{-29}$e.cm (Engel et al., 2013; Safronova et al., 2018). However, due to the complexity of this nucleus, the theoretical calculations on the Schiff moment are contradictory, even though the different methods include much of the same physics. In contrast, other nuclei, such as ^{225}Ra or ^{129}Xe, have allowed more reliable calculations (Engel et al., 2013). Since the Schiff moment is enhanced in octupole-deformed nuclei, ^{225}Ra has been the focus of experimental interest in EDM studies due to its asymmetric shape (two to three orders of magnitude of enhancement) and nuclear spin $1/2$, making its nuclear orientation insensitive to stray quadrupole fields (Engel et al., 2013). Despite this, the current Ra EDM measurements have not yet reached the desired sensitivity to P, T-odd interactions comparable to the ^{199}Hg experiment (Engel et al., 2013; Flambaum and Dzuba, 2020).

To further enhance the sensitivity to P, T-odd interactions, polar molecules appear as promising candidates due to the strong internal electric field (orders of magnitude higher than the electric field in atoms or externally applied electric fields). Polar molecules also exhibit close-lying rotational levels of opposite parity, further enhancing the appearance of P, T-odd interactions (Flambaum and Dzuba, 2020). This mixing between opposite parity rotational doublets further increases the sensitivity relative to the case of atoms between three to five orders of magnitude (Engel et al., 2013). As such, studies in diatomic polar molecules composed of heavy octupole-deformed nuclei would lead to the biggest enhancement in the Schiff moment.

Flambaum and Dzuba (2020) summarized a list of the different nuclei that could be used to study the Schiff moment. Unfortunately, most of these nuclei are non-stable, making their study restrained to radioactive facilities capable of their production.

The first experimental study on molecular electronic levels for radioactive molecules was performed in 2018, on molecules of RaF isotopologues (molecules containing different isotopes of Ra) (Garcia Ruiz et al., 2020). The present work builds further on that first study, by establishing for the first time the excited energy levels up to 30.000 cm^{-1} in molecules of ^{226}Ra^{19}F. The data were obtained in an experiment at the collinear resonant ionization spectroscopy (CRIS) beam line at ISOLDE-CERN, performed in November 2021. The obtained excitation energies are used to assess the predicted power of quantum chemistry methods for molecules made of alkaline earth metals (Garcia Ruiz and Wilkins, 2020; Athanasakis-Kaklamanakis et al., 2021).

Chapter 2

Theory

2.1 Molecular orbital theory

The most common approach to describe the molecular wave function is through the linear combination of atomic orbitals method (LCAO). In this method, **for a diatomic molecule**, two atomic orbitals of atoms a and b can interact in-phase or out of phase to form a bonding (ψ or ψ_+) or anti-bonding (ψ^* or ψ_-) orbital, respectively. Eq 2.1 shows the molecular wavefunction as a superposition of the two atomic orbitals (Atkins et al., 2014),

$$\psi_\pm = N_\pm(\psi_a \pm \psi_b) \tag{2.1}$$

where $N_\pm$ is a normalization factor. The formed molecular orbitals that have a cylindrical symmetry around the internuclear axis are called a σ orbital, as they have a zero orbital angular momentum around the internuclear axis. This is the type of orbitals formed by s and p_z atomic orbitals. Similarly, molecular orbitals that are perpendicular to the internuclear axis and have a value of one orbital angular momentum are called π orbitals, being formed by p_x and p_y atomic orbitals. Figure 2.1 shows a representation of the molecular orbitals formed on Li_2.

The electronic configuration is obtained by progressively filling the molecular orbitals with electrons, following the Pauli exclusion principle. The electronic orbital angular momentum (Λ) is obtained by the sum of the individual electron orbital angular momentum λ_i,

$$\Lambda = \sum_i \lambda_i \tag{2.2}$$

The number of electrons and the way how they couple in the molecular orbital will define the electronic state that is formed. For example, for one electron in a π molecular orbital, the orbital angular momentum is $\Lambda = \pm 1$, and the electronic state is called a Π state. For two electrons in a π molecular orbital $\Lambda = \pm 2, 0$, a Δ ($|\Lambda| = 2$) or Σ ($\Lambda = 0$) electronic state is formed. Similarly to Λ, the electronic spin angular momentum S is equal to the sum of the individual spins, that is (Brown and Carrington, 2003),

$$S = \sum_i s_i \tag{2.3}$$

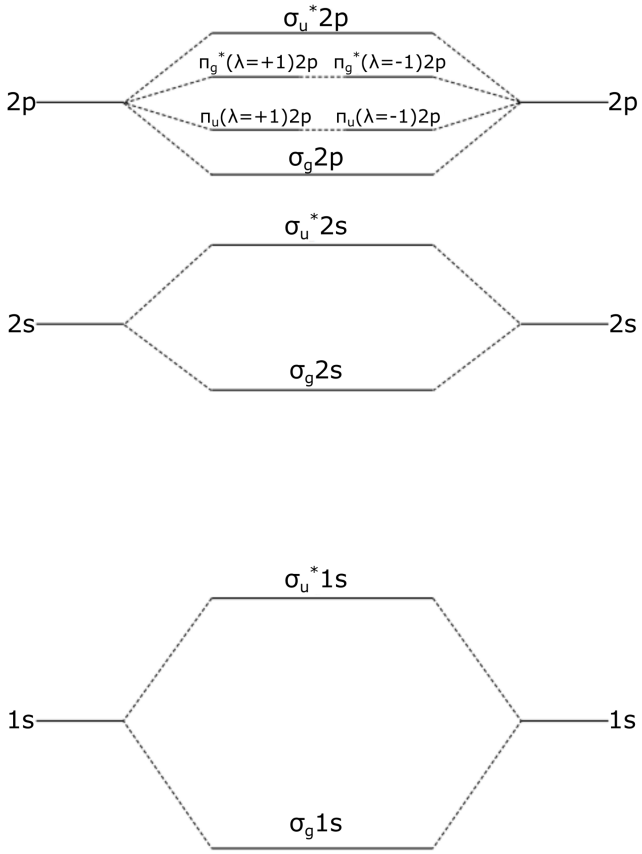

Figure 2.1: Molecular orbital energy level diagram for the homonuclear diatomic molecules of the first row of the periodic table. Taken from (Brown and Carrington, 2003)

The resulting spin multiplicity, $2S+1$, is indicated as a prefix superscript, while the spin-orbit coupling ($\Omega = |\Lambda + S|$) is expressed as a subscript. The excited states with the same spin multiplicity will be labeled in alphabetic order as A, B, C, etc. Similarly, the ground state is labeled X (Brown and Carrington, 2003). As such, the first excited electronic state (A) made out of one electron ($S = 1/2$) in a π orbital ($\Lambda = 1$) will form a $A^2\Pi_{1/2}$ or $A^2\Pi_{3/2}$ state.

2.2 Molecular Hamiltonian

We can describe the energy of a diatomic molecule based on three internal energy levels: rotational, vibrational, and electronic. Due to the vibrational motion of the constituent nuclei, each electronic state ($\Delta E_{elec} \approx 15,000$ cm^{-1}) is split into a closely spaced set of additional energy levels, referred to as the vibrational structure ($\Delta E_{vib} \approx 500$ cm^{-1}). Similarly, each vibrational level is further composed of even closer spaced rotational levels ($\Delta E_{rot} \approx 1$ cm^{-1}), and in the case of open-shell molecules, by fine and hyperfine states ($\Delta E_{fs} \approx 100$ cm^{-1} and $\Delta E_{hfs} \approx 0.01$ cm^{-1}) (Brown and Carrington, 2003). As such, the effective Hamiltonian for a molecule in the absence of external fields is given by,

$$H = H_{elec} + H_{vib} + H_{fs} + H_{rot} + H_{hfs} \tag{2.4}$$

The energy of an electronic energy state (T_{elec}) is not described by any standard equation, except in the case of Rydberg states. However, for the purpose of rotational-vibrational

spectroscopy, we are going to focus on the vibrational and rotational energy levels. Figure 2.2 shows an schematic representation of the energy levels of a diatomic molecule.

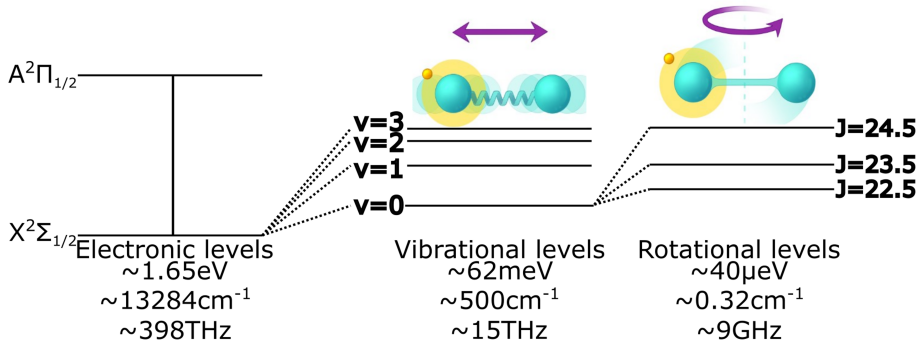

Figure 2.2: Schematic representation of a diatomic molecule energy levels using RaF ground and first excited states. Adapted from Sonja Kujanpää, JYU

Vibrational energy

The energy given by the vibrational modes of the constituent nuclei in the molecule can be obtained from the anharmonic oscillator, which describes the potential between the two atoms by the harmonic oscillator and a correction power series of second order to compensate for the infinite restoring force with increasing distance. An alternate potential that allows the wave equation to be solved rigorously is the Morse potential. Nevertheless, the vibrational energy $(G(v))$ given by the anharmonic oscillator (truncated to the second order) or the Morse potential is,

$$G(v) = \omega_e(v + 1/2) - \omega_e x_e(v + 1/2)^2 \tag{2.5}$$

where v is the vibrational quantum number ($v = 0, 1, 2, ...$), ω_e is the harmonic vibrational frequency, and x_e is a positive dimensionless parameter called the anharmonic vibrational constant. The latter expresses some of the effects of nonzero higher derivatives of the inter-nuclear potential energy function. Furthermore, $\omega_e x_e$ can be used to estimate the energy required to break the molecular (A-B) bond (Lefebvre-Brion and Field, 2004).

Rotational energy

The rotational energy $(F(J))$ is represented by a truncated series of $J(J + 1)$ as (Lefebvre-Brion and Field, 2004),

$$F(J) = B_v J(J + 1) - D_v[J(J + 1)]^2 \tag{2.6}$$

where J is the rotational quantum number ($J = 0, 1, 2, ...$ or $J = 1/2, 3/2, 5/2, ...$), B_v is the rotational constant for the v-th vibrational level, and D_v is the centrifugal distortion constant (typically on the order of $\approx 10^{-6}B_v$) for the v-th vibrational level. Due to its dependence on J, the energy separation between neighboring levels increases as J increases (Atkins et al., 2014). This energy is approximated using the non-rigid rotor model, where the inter-nuclear distance, and the moment of inertia, will increase with increasing rotation (Brown and Carrington, 2003).

During a vibration, the moment of inertia of molecule changes, affecting its rotation. As such, B_v and D_v are weakly dependent on the vibrational levels, giving rise to a rotational-vibrational coupling correction term proportional to $(v + 1/2)$ (Brown and Carrington, 2003),

$$\begin{aligned} B_v &= B_e - \alpha_e(v + 1/2) + ... = \frac{16.85763}{\mu(\text{amu})R_e^2(\text{Å}^2)} - \alpha_e(v + 1/2) + ... \\ D_v &= \frac{4B_v^3}{\tilde{\nu}} = 8B_v^3\pi c\sqrt{\frac{\mu}{k}} \end{aligned} \tag{2.7}$$

where α_e is the rotational-vibrational coupling constant, usually positive and of the order of $10^{-2}B_e$, $\tilde{\nu}$ is the vibrational wavenumber of the bond, k is the second derivative of the inter-nuclear potential energy function, and μ is the reduced mass of the molecule. It is worth noting that, despite the weak dependence of B_v and D_v with the vibrational levels, they are strongly dependent on the electronic state. Furthermore, since B_v is related to the equilibrium inter-nuclear distance (R_e), it is possible to retrieve the separation between the two atoms from B_v (Lefebvre-Brion and Field, 2004).

Hund's cases

Molecules are complex systems characterized by many different angular momenta. Hund's cases are idealized situations that help to understand the energy levels of diatomic molecules by considering the various ways these angular momenta can couple (Bethe, 1933). The different angular momenta involved are:

- $\boldsymbol{L}$ is the total electronic orbital angular momentum, and its projection on the internuclear axis is Λ.
- $\boldsymbol{S}$ is the total electronic spin angular momentum, and its projection on the internuclear axis is Σ.
- $\boldsymbol{J_a} = \boldsymbol{L} + \boldsymbol{S}$ is the total electronic angular momentum, with projection $\Omega = |\Lambda + \Sigma|$ on the internuclear axis.
- $\boldsymbol{R}$ is the rotational angular momentum of the nuclei with respect to the center of mass of the molecule.
- $\boldsymbol{J} = \boldsymbol{R} + \boldsymbol{J_a}$ is the total angular momentum of the system (excluding nuclear spin).
- $\boldsymbol{N} = \boldsymbol{R} + \boldsymbol{L} = \boldsymbol{J} - \boldsymbol{S}$ is the total angular momentum of the system excluding electron (and nuclear) spin.

In total, there are five different cases denoted by the letters (a) through (e), defining a set of good quantum numbers for each case (see Table 2.1), where A is the spin-orbit coupling constant (see Section 2.2) and η denotes all other quantum numbers not expressed explicitly, e.g., electronic and vibrational. However, most molecules can be described using Hund's cases (a) and (b) (Brown and Carrington, 2003). As such, this work will only focus on these two.

Table 2.1: Hund's coupling cases. Taken from (Brown and Carrington, 2003).

Coupling case	Good quantum numbers	Requirements	Comment
(a)	η, Λ, S, Σ, J, Ω	$A\,\Lambda \gg BJ$	$H_{spin-orbit} \gg H_{rotational}$
(b)	η, Λ, N, S, J	$A\,\Lambda \ll BJ$	$H_{spin-orbit} \ll H_{rotational}$
(c)	η, J_a, Ω, J	$A\,\Lambda \gg \Delta E_{elec}$	$H_{spin-orbit} \gg H_{electronic}$
(d)	η, L, R, N S, J	$BJ \gg \Delta E_{elec}$	$H_{rotational} \gg H_{electronic}$
(e)	η, J_a, R, J	$A\,\Lambda \gg BJ \gg \Delta E_{elec}$	$H_{spin-orbit} \gg H_{rotational} \gg H_{electronic}$

Hund's coupling case (a)

The most common coupling case is Hund's case (a), where the spin-orbit electronic interaction is stronger than the rotational interaction of the molecule around the internucleon axis (Hollas, 2004). In this case, the electron spin $\boldsymbol{S}$ and orbital moment $\boldsymbol{L}$ are coupled to a total electron angular momentums $\boldsymbol{J_e}$. This angular momentum is strongly coupled to the internuclear axis, such that all spin projections (Λ, Σ, and Ω) are well-defined. In this case, the total electronic angular momentum $\boldsymbol{J_e}$ will couple to the rotational angular momentums $\boldsymbol{R}$ to form the total molecular angular momentum $\boldsymbol{J}$. Figure 2.3 shows a schematic representation of the angular momentum coupling in Hund's case (a).

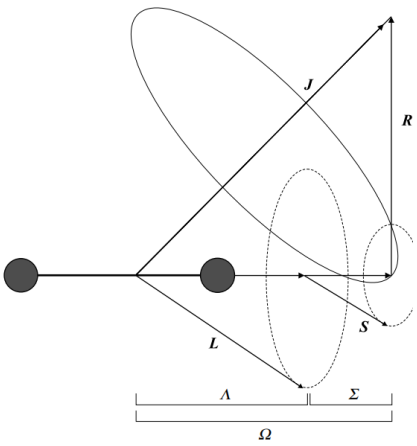

Figure 2.3: Vector coupling diagram for Hund's case (a). Taken from (Brown and Carrington, 2003).

The precessions of $\boldsymbol{L}$ and $\boldsymbol{S}$ have two equal and opposite senses so that the projections also have magnitudes $\pm\Lambda, \pm\Sigma$, producing a degeneracy in Λ and Ω called Λ- and Ω-doubling. In a good case (a), there are $2S+1$ fine structure states defined in terms of their Ω quantum number. Each of these levels has a rotational pattern with energies $BJ(J+1)$ and the same rotational constant (Lefebvre-Brion and Field, 2004), being $J = \Omega$ the lowest rotational level. As J increases, case (a) becomes less appropriate (Brown and Carrington, 2003).

Hund's coupling case (b)

When $\Lambda = 0$ or the spin-orbit coupling is weaker than the rotational interaction of the molecule and $S \neq 0$, then the total electron spin $\boldsymbol{J_e}$ is not a good quantum number. In this case, the electron orbital momentum $\boldsymbol{L}$ will couple to the rotational angular momentum $\boldsymbol{R}$ rather than to the electron spin $\boldsymbol{S}$. This coupling of $\boldsymbol{L}$ and $\boldsymbol{R}$ leads to a new total angular momentum $\boldsymbol{N}$, which will then couple to the electron spin $\boldsymbol{S}$ to form the total molecular angular momentum

$\boldsymbol{J}$. For Hund's case (b), each vibrational level is composed of a rotational pattern with energies $BN(N+1)$, starting at $N = \Lambda$. Each $N-$value is $2S+1$ degenerated (values of J varies between $N - S \leq J \leq N + S$) (Brown and Carrington, 2003). This degeneracy is lifted by the spin-rotational term. However, for $N = 0$ or $N = 1/2$, the degeneracy is not lifted as J can't be negative (Herzberg and Mrozowski, 1951).

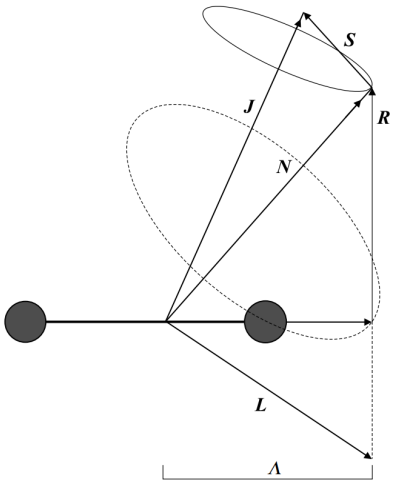

Figure 2.4: Vector coupling diagram for Hund's case (b). Taken from (Brown and Carrington, 2003).

Spin part of the Hamiltonian

For an open shell molecule ($S > 0$), relativistic terms due to the interaction between the electron spin ($\boldsymbol{S}$), its orbital angular momenta ($\boldsymbol{L}$), the spin of other electrons, and the rotational angular momenta ($\boldsymbol{R}$) of the nuclei must also be considered, as they lift the spin degeneracy and produce a zero-field splitting. These effects can be divided into three parts (Lefebvre-Brion and Field, 2004):

- **Spin-orbit interaction** (H_{SO}): Interaction between the spin ($\boldsymbol{S}$) and orbital angular momenta ($\boldsymbol{L}$) of the electrons.
- **Spin-rotation interaction** (H_{SR}): Interaction between the electron spin and the magnetic field created by nuclear motion (rotational angular momenta of the nuclei).
- **Spin-spin interaction** (H_{SS}): Interaction between the spins of different electrons.

Among these, the $\boldsymbol{H_{SS}}$ can be ignored for RaF since it only possesses one valence electron.

Spin-orbit interaction

The first-order contribution of the spin-orbit interaction ($\boldsymbol{L} \cdot \boldsymbol{S}$) can be defined in terms of A, the spin-orbit coupling constant, as,

$$\langle \Lambda, \Sigma, S, \Omega, v \,|\mathbf{H}_{\mathrm{SO}}|\, \Lambda, \Sigma, S, \Omega, v \rangle = A_{\Lambda,v} \Lambda\Sigma \tag{2.8}$$

where v is the v-th vibrational level. For $\Lambda > 0$, this operator produces an equal space fine structure proportional to $A\Lambda$. The sign of A will determine the order of the fine-structure

state, e.g., considering a $^2\Pi$ state, the sub-state $^2\Pi_{3/2}$ will be higher (lower) in energy than $^2\Pi_{1/2}$ for $A > 0$ ($A < 0$) (Brown and Carrington, 2003). However, the second-order spin-orbit effect can distort this equidistant pattern. This level shift, for $\Lambda > 0$ states, can be proportional to $\Lambda\Sigma$ or to $3\Sigma^2 - S(S+1)$ (Lefebvre-Brion and Field, 2004). It is worth noting that the second-order spin-orbits effect is unobservable for $^1\Sigma$ and $^2\Sigma$ states (Lefebvre-Brion and Field, 2004). Furthermore, the second-order spin-orbits effect is indistinguishable from the spin-rotational contribution for $^2\Pi$ states. Thus, they are often en-globe as one or the other (Veseth, 1971).

Spin-rotational interaction

Due to the bigger mass of the nuclei ($M = Z+N$) compare to the electron (M_e), their angular velocity is at least m/M (1/1836) times smaller than the angular velocity of electrons. As such, the spin-rotation interaction is very small compared to the spin-orbit interaction, except for light molecules (Lefebvre-Brion and Field, 2004). This allows in most cases to defined a given electronic level as Hund's case (a). For this case, the spin-rotation interaction is given in terms of the spin-rotation coupling constant (γ) as,

$$\boldsymbol{H_{SR}} = \gamma \boldsymbol{R} \cdot \boldsymbol{S} = \gamma(\boldsymbol{N} - \boldsymbol{L}) \cdot \boldsymbol{S} \tag{2.9}$$

As such, the diagonal terms are,

$$\left\langle \Lambda S \Sigma \Omega \left| \mathbf{H}^{\mathrm{SR}} \right| \Lambda S \Sigma \Omega \right\rangle = \gamma \left[\Omega\Sigma - S(S+1) \right] \tag{2.10}$$

However, due to the weak coupling between the electron spin and the nuclear rotation axis, the contribution of $\boldsymbol{H_{SR}}$ is small for case (a). Alternatively, the spin-rotational term can be denoted for case (b) as,

$$\boldsymbol{H_{SR}} = \gamma \boldsymbol{N} \cdot \boldsymbol{S} \tag{2.11}$$

where the diagonal terms are given by,

$$\langle N J S \Lambda \left| \mathbf{H}_{\mathrm{SR}} \right| N J S \Lambda \rangle = (\gamma/2)[J(J+1) - N(N+1) - S(S+1)] \tag{2.12}$$

It is worth noting that perturbations between electronic states due to $\boldsymbol{H_{SR}}$ are so weak that they are virtually undetectable (comparable to hyperfine perturbation for light molecules) (Lefebvre-Brion and Field, 2004).

Λ-doubling terms for Π electronic states

As aforementioned in Section 2.2, states with $\Lambda \neq 0$ present a double degeneracy, forming what is called Ω-doublets or Λ-doublets (for non-rotating molecules). However, for rotating molecules, the degeneracy is lifted by the off-diagonal terms of the rotational and spin-orbit Hamiltonian's, splitting the double degenerate J values (J^+ and J^-) with a strength proportional to J (Herzberg and Mrozowski, 1951). This phenomenon is called Λ-doubling and is originated from the admixture of the rotational levels of the degenerate electronic state (e.g., Π state) with the corresponding levels of a Σ electronic state. Since each Σ level is non-degenerate and has a defined parity ($+$ or $-$), they will interact with only one of the two degenerate components of Ω, namely the one with the same parity, shifting this component from its partner of opposite parity (Brown and Carrington, 2003). In general, the magnitude

of the Λ-splitting will be around a couple of GHz. Only in special cases and high J it can reach a few cm^{-1} (Herzberg and Mrozowski, 1951).

Λ-doubling effect is largest for Π electronic states. This is because the coupling between the Π and Σ is produced by a second-order mixing given by the spin–orbit coupling and the rotational electronic Coriolis term. Whereas in Δ-states, this Λ-doubling arises from fourth-order mixing with a remote Σ state through an intermediate Π state. Thus, in second-order perturbation theory, we can write the Hamiltonian for Λ-doubling for a Π state as,

$$H_{\mathrm{LD}}(R) = \sum_{q=\pm 1}^{\prime} \exp(-2\mathrm{i}q\phi)\left[-o(R)\mathrm{T}^2_{2q}(\boldsymbol{S},\boldsymbol{S}) + p(R)\mathrm{T}^2_{2q}(\boldsymbol{S},\boldsymbol{N}) - q(R)\mathrm{T}^2_{2q}(\boldsymbol{N},\boldsymbol{N})\right] \tag{2.13}$$

where $\mathrm{T}^2_q(\boldsymbol{S},\boldsymbol{S})$ represents the component q of a spherical tensor of rank 2 of the operator resulting from the tensor product between two spin operators, ϕ is the electron orbital azimuthal angle, and the exponential ensures that only the matrix elements which connect components $|\eta,\Lambda=+1\rangle$ with $|\eta,\Lambda=-1\rangle$ are non-zero (Brown and Carrington, 2003). o, p and q are three Λ-doubling parameters, from which p is only non-zero for $S>0$, and o is only non-zero for $S>1/2$ (Brown and Merer, 1979).

Rotational-vibrational spectrum

A rotational-vibrational-electronic spectrum is a collection of transitions between an upper state and a lower state, always denoted by a single prime ($'$) and a double prime ($''$), respectively (Lefebvre-Brion and Field, 2004). The energy of each of these transitions is given by the sum of the electronic (T_o), vibrational (T_o), and rotational (F_ν) energy levels. Figure 2.5 shows a schematic representation of the contribution of each energy level for the ground and exited state of a molecule.

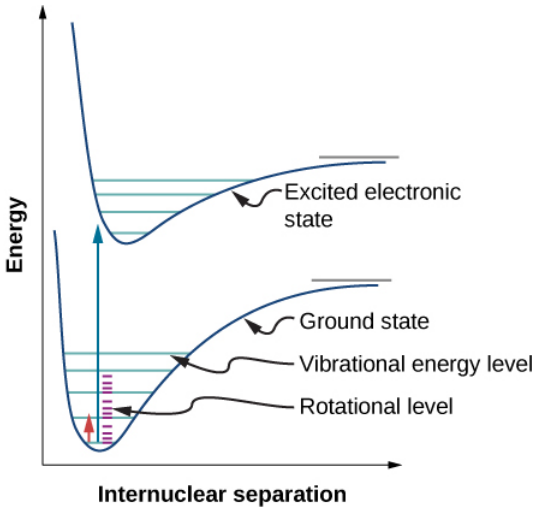

Figure 2.5: Energy contributions in a diatomic molecule: electronic, vibrational, and rotational. Taken from LibreTexts (2023)

Thus, the ground ($E''_{e'',v'',J''}$) and exited state ($E'_{e',v',J'}$) energies are given as,

$$\begin{aligned} E'_{e',v',J'} &= T'_0 + G'(v') + F'_{v'}(J') \quad \text{Upper state} \\ E''_{e'',v'',J''} &= T''_0 + G''(v'') + F''_{v''}(J'') \quad \text{Lower state} \end{aligned} \tag{2.14}$$

while the retrieved spectrum would be given by the difference between the two,

$$\Delta E = (T' - T'') + [G'(v') - G''(v'')] + [F'_{v'}(J') - F''_{v''}(J'')]. \tag{2.15}$$

Since the difference in energy between two different electronic energy levels will only be seen as a shift in energy in the retrieved spectrum, we can focus only on the rotational-vibrational components.

2.3 Selection rules and branches

Electronic and vibrational selection rules

The selection rules that govern the transition between electronic levels in linear molecules, according to the conservation of angular momentum and photon spin (S = 1), is given by (Atkins et al., 2014),

$$\Delta\Lambda = 0, \pm 1; \;\; \Delta S = 0; \;\; \Delta\Sigma = 0; \;\; \Delta\Omega = 0, \pm 1; \tag{2.16}$$

These selection rules limits the electronic levels that can be accessed from a given initial state, e.g. for a molecule with a Σ ground state any Δ state can only be (allowed) accessed using an Π intermediate state.

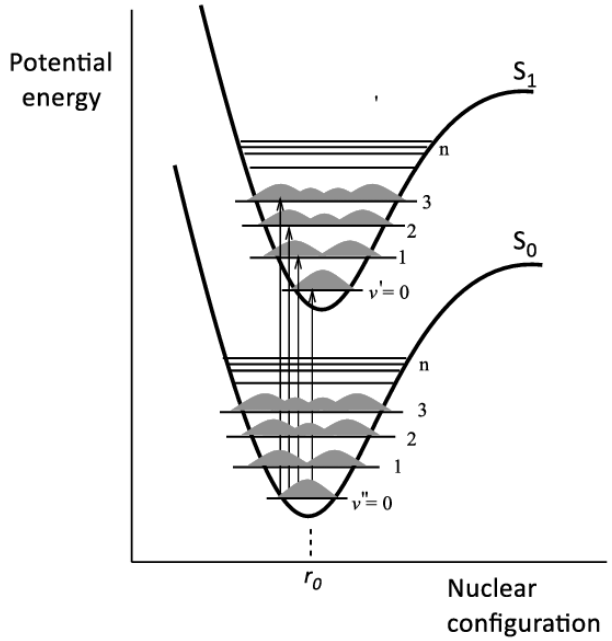

Figure 2.6: Diagram of the transition of the ground state in a given vibrational state to a different vibrational state in the excited state. The vibrational levels are represented as wavefunctions and absorption electronic transitions are represented by vertical arrows. Taken from (Nano, 2015).

Furthermore, any electronic transition can be accompanied by a simultaneous change in the vibrational state of the molecule, giving rise to a vibrational structure (Atkins et al., 2014). Figure 2.6 shows a schematic representation of the different transitions possible from a given vibrational state in the ground state (ν'') to a different vibrational state in the exited state (ν'). As it can be seen, unlike the harmonic oscillator, no selection rule forbids the transition between vibrational states. In this case, the transition intensity is governed by the Franck–Condon principle.

The Franck-Condon principle states that the most intense molecular transition between vibrational states is the one in which the molecular dynamic state is conserved. This has led the Franck–Condon principle to be popularly summarized as the vertical transition principle, in which the strongest transition will be given to the vibrational state immediately above the initial electronic state (Atkins et al., 2014). However, the refined picture from quantum mechanics explains that the most intense transition would be the vibrational state whose wave function resembles the initial one the most. Figure 2.7 shows two cases in which the most intense vibrational transition state can be either an unexcited (a) or exited (b) state depending on the inter-nuclear distance difference between the initial and final state. It is worth noting that transitions to other vibrational levels are also allowed but with a lower intensity (see Figure 2.6, where the fundamental transition is a $\nu'' = 0 \rightarrow \nu' = 0$ but other transitions are still allowed).

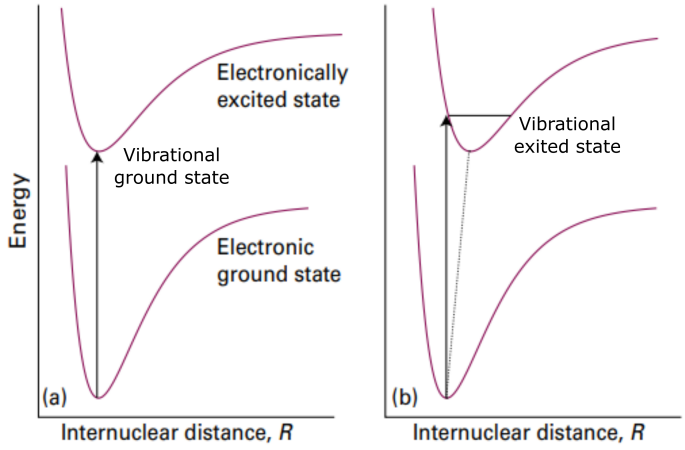

Figure 2.7: The Franck-Condon principle shows that the most intense vibronic transition is from the ground vibrational state to the vibrational state lying vertically above it. On a), the equilibrium bond lengths are equal, leaving the vibrational state of the molecule unchanged. On the other hand, the difference between the equilibrium bond length on b) produces a vibrational excitation. Taken from (Atkins et al., 2014).

Rotational selection rules

For a diatomic molecule, the selection rule for an electric dipole allowed transition between two rotational energy levels is $\Delta J = 0, \pm 1$. Since the rotational-vibrational spectrum consists of a large number of closely spaced components, the retrieved spectrum is often called a band spectrum and it can be divided into three different branches depending on the difference of the rotational quantum number between the lower and the upper states (Atkins et al., 2014). Transitions that involve a $\Delta J = J' - J'' = +1$ will need an extra amount of energy and would

be present on the right side of the spectrum called the R branch. Similarly, the transitions that involve a $\Delta J = 0$ and -1 are part of the Q and P branches, respectively, e.g., $P(J)$ is used to denote a transition that belongs to the P branch and whose initial rotational quantum number is $J'' = J$. This difference in energy between branches can be seen (neglecting D' and D'' contributions) in,

$$\begin{aligned}
\tilde{v}_{\mathrm{P}}(J) &= \tilde{v} - \left(\tilde{B}' + \tilde{B}''\right) J + \left(\tilde{B}' - \tilde{B}''\right) J^2 \\
\tilde{v}_{\mathrm{Q}}(J) &= \tilde{v} + \left(\tilde{B}' - \tilde{B}''\right) J(J+1) \\
\tilde{v}_{\mathrm{R}}(J) &= \tilde{v} + \left(\tilde{B}' + \tilde{B}''\right) (J+1) + \left(\tilde{B}' - \tilde{B}''\right) (J+1)^2
\end{aligned} \tag{2.17}$$

As it can be seen, the separation between the lines in the P and R branches depends on the difference between B of the two levels. It is worth noting that some rovibrational spectrum does not present a Q-branch if transitions with $\Delta J = 0$ are forbidden. The latter are only allowed for a molecule with a angular momentum about its inter-nuclear axis (Atkins et al., 2014). Thus, in diatomic molecules, the Q-branch is not present between transitions of Σ states, but it is present between Σ and Π states. Figure 2.8 shows an example spectrum of rotational-vibrational transitions. The intensity distribution of each of these branches reflects both the rotational levels populations and the magnitude of the transition moment. This intensity increases with J, passing through a maximum and tailing off as J increases. The main reason for this behavior is the compensation between the population distribution given by the Boltzmann distribution and the degeneracy of each rotational level. Each rotational level consists of $2J + 1$ degenerate states, allowing a bigger population distribution with increasing J. However, the population of a state decreases exponentially as its energy increases, following a Boltzmann distribution,

$$N_J = N g_J e^{-E_J/kt} \tag{2.18}$$

where N is the total number of molecules in a particular rotational level with angular momentum J, and g_J is the degeneracy of the J level (Atkins et al., 2014).

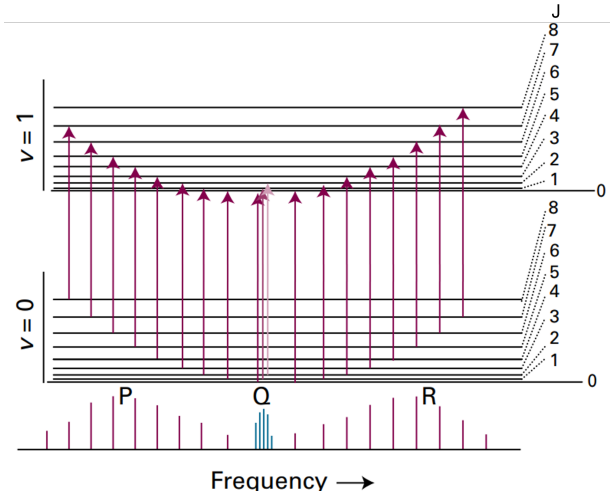

Figure 2.8: Formation of P, Q, and R branches in a vibration–rotation spectrum. The intensities reflect the populations of the initial rotational levels and magnitudes of the transition moments. Taken from (Atkins et al., 2014)

Depending on the sign of $B' - B''$, at a given J'', the lines in either the R or the P branch will get close and closer, piling up in a "bandhead" and continuing in the opposite direction, in frequency, at higher J. This happens at sufficiently high values of J, when the $(J+1)^2$ will dominate the linear term $(J+1)$(Atkins et al., 2014). Figure 2.9 shows the appearance of the bandhead in the R branch for a $^{102}Ru^{12}C\ ^1\Pi \leftarrow X^1\Sigma^+$ transition since $B' - B'' < 0$. Similarly, the bandhead would appear in the P branch if $B' - B'' > 0$.

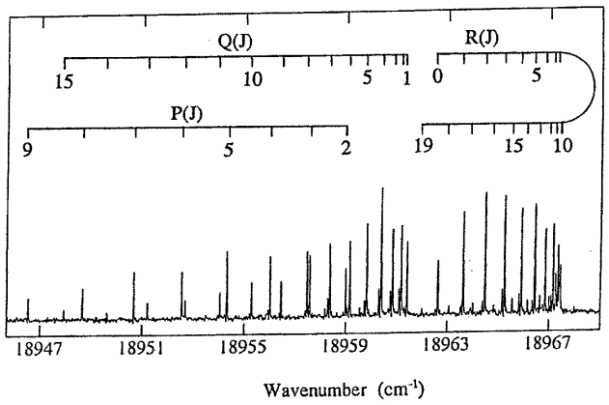

Figure 2.9: $^{102}Ru^{12}C\ ^1\Pi \leftarrow X^1\Sigma^+$ transition, The assignments of rotational lines are distinguished by vertical tie lines. The lines in each R, Q, and P rotational branch connect with a different horizontal tie line. The bandhead occurs in the R branch near $J'' = 9$. Taken from (Langenberg et al., 1998).

2.4 Electric dipole moment (EDM)

The combined violation of charge conjugation symmetry (C) and parity symmetry (P) (CP-violation) has been a focus of research since the '50s due to its importance on the different unresolved problems in physics, e.g., baryogenesis problem (Purcell and Ramsey, 1950). One of the approaches to measure it is through the measurement of a permanent EDM in a given system. In the case of neutral atoms, the presence of a nuclear EDM is hindered by the re-arrangement of its constituents, screening the electric field and keeping the system stationary according to the Schiff theorem (Liu et al., 2006).

Schiff theorem

The Schiff theorem is the mathematical proof performed by L. I. Schiff in 1963 showing that for a non-relativistic point-charged quantum system, electric dipoles in an external electrostatic potential of arbitrary form are completely shielded and therefore can not be observed, even if such electric dipole moment would be present in the point-charged system (Schiff, 1963). Since the presence of an EDM in any physical system would require the existence of P, T-violating interactions in nature, the search for such EDM is an important route to study these yet non-observed interactions and prove new physics beyond the Standard Model (Auerbach and Zelevinsky, 2009). One approach to search for the existence of an EDM is to search for an EDM in atoms and molecules where the nuclei inside them are non-point-like quantum systems interacting with relativistic electrons. Therefore, they could have an EDM.

For nuclei or electrons inside an atom or molecule, the basic assumptions of the Schiff theorem are not fulfilled since the atomic nuclei have a finite size, the electrons have a relativistic behavior, and their interaction with the nuclei is not purely electrostatic. As such, an atomic (or molecular) EDM would be measurable due to a combination of these effects (Liu et al., 2006). In the atomic case, an EDM can be produced due to any of the following P, T-odd interactions (Ginges and Flambaum, 2004),

- Intrinsic EDM of an unpaired electron: the electron EDM (eEDM) can interact with the atomic field, inducing an atomic EDM greater than a single eEDM.
- P, T-odd electron-nucleon interaction.
- Intrinsic EDM of a unpaired nucleon.
- P, T-odd nucleon-nucleon interaction: this interaction can induce P, T-odd nuclear moments that can greatly exceed the moments of a single nucleon (Haxton and Henley, 1983; Ginges and Flambaum, 2004).

The atomic and molecular studies in search for CP violation can be broadly classified into two categories: studies of paramagnetic systems with an unpaired electron spin and diamagnetic systems with close electron shells but nonzero nuclear spin (Khriplovich and Lamoreaux, 2012; Safronova et al., 2018). Paramagnetic systems are particularly sensitive to effects that depend explicitly on electron spin, such as the eEDM and electron-nucleus interaction. These systems can be used to extract the electron EDM. On the other hand, diamagnetic systems are more sensitive to effects that depend explicitly on the nuclear spin, such as the nuclear P, T violation effects, the nucleons EDM, and some other types of semileptonic interactions. These systems allow the extraction of hadronic EDM (Khriplovich and Lamoreaux, 2012; Safronova et al., 2018).

To observe an EDM, one has to measure the interaction of the EDM with an electric field. Considering that the internal electric field in polar molecules is orders of magnitude larger than any external field, e.g., 10^9 V/cm for Thallium fluoride (Khriplovich and Lamoreaux, 2012), polar molecules have been identified as the most sensitive probes to measure an EDM (Flambaum and Dzuba, 2020). This internal electric field can mix the opposite parity rotational doublets levels present in molecules, given by the Stark Hamiltonian in the first order. Due to the small energy gap of these doublets, associated with the rotational Λ-double structure (Safronova et al., 2018), there is a dramatic increase in its sensitivity to P, T-violating interactions (Flambaum and Dzuba, 2020). This increase, relative to the case of atoms in lab-scale E fields, is typically between three to five orders of magnitude in observable P, T energy shifts. Thus, molecules are a promising field to increase the sensitivity of EDM studies (Kozlov and Labzowsky, 1995; Safronova et al., 2018).

In paramagnetic molecules, the presence of a molecular EDM due to P, T-odd electron-nucleon interactions are, in most theoretical models, far away from the experimental limits (Khriplovich and Lamoreaux, 2012), making eEDM searches more appealing for this type of system. However, the study of paramagnetic molecules is challenging since they are very reactive, thermodynamically unstable, and there is limited information about their characteristics (Khriplovich and Lamoreaux, 2012). As such, EDM studies due to P, T-odd nuclei interactions have become the focus of experimental interest and produced several recent developments (Engel et al., 2013; Ginges and Flambaum, 2004).

P, T-violating nuclear moments

EDMs in atoms and molecules can manifest themselves through the presence of anomalous electric or magnetic nuclear moments. These moments are considered zero if P (parity) and T (time reversal) symmetries are not violated. So, the observation of such anomalous moments would be an indication of the violation of these symmetries. These anomalous nuclear moments are the Schiff moment, the electric octupole moment, and the magnetic quadrupole moment. The nature of the operator responsible for the P, T-mixing in each of these moments constraint the Schiff moment to nuclei with spin $I \geq 1/2$, the octupole moment on $I \geq 3/2$, and the magnetic quadruple moment on $I \geq 1$ (due to the triangle rule for the addition of angular momenta) (Ginges and Flambaum, 2004). Due to the higher rank of the electric octupole moment, this mixes electronic states of higher angular momentum than the Schiff moment, producing a very small atomic EDM (Ginges and Flambaum, 2004). This means that the atomic EDM produced by the electric octupole moment is considerably smaller than the Schiff moment. As such, it would not be considered in the present work.

Schiff moment

The Schiff moment is the first non-vanishing term (third order) in the expansion of the nuclear electromagnetic potential after including the screening of the atomic electrons (Sen'kov et al., 2007; Flambaum, 2019). This is defined as,

$$\vec{S} = \vec{S}^{ch} + \vec{S}^{N} \tag{2.19}$$

where $\vec{S}^{ch}$ is the contribution to the Schiff moment due to the charge distribution of the nucleus, and $\vec{S}^{N}$ is due to the EDM of the nucleons. The former can only be induced by an effective P, T violating inter-nucleon interaction that induces the mixing of opposite parity wave functions (Engel et al., 2013; Ginges and Flambaum, 2004). Furthermore, it was shown by Sushkov et al. (1984) that the contributions of the P, T-odd forces to the Schiff moment is ~ 40 times larger than the contribution of the nucleon EDM. As such, the Schiff moment is usually represented as,

$$\mathbf{S} = \vec{S}^{ch} = \frac{e}{10}\left[\langle r^2\mathbf{r}\rangle - \frac{5}{3}\langle r^2\rangle_{ch}\langle\mathbf{r}\rangle\right] \tag{2.20}$$

where $\langle r^n\rangle$ are the moments of the nuclear charge density ρ, and the second term comes from the electron screening, composed by $\langle r^2\rangle_{ch}$ the nuclear mean square charge radius and the nuclear EDM $d = e\langle\mathbf{r}\rangle$ (Flambaum, 2019). It is worth noting that Eq 2.20 is only an approximation. Corrections from nuclear quadrupole deformation, relativity in electronic wave functions, and more subtle electron-nucleon interactions have to be included. However, the entire form of this equation has not been entirely settled (Engel et al., 2013).

The Schiff moment polarizes the atom and produces an atomic EDM directed along the nuclear spin. The presence of such permanent EDM, in either atoms or molecules, would be evidenced by a linear Stark effect (Ginges and Flambaum, 2004). However, the expected EDM is very small. As such, the studies of the Schiff moment have been performed in systems that enhance its effects (Flambaum and Dzuba, 2020).

The Schiff moment is enhanced in nuclei with a close level of opposite parity with the same angular momentum as the ground state (Sushkov et al., 1984). The nuclei's collective behavior can further enhance the Schiff moment. **However, the biggest enhancement is present in nuclei that satisfy the two previous requirements (octupole deformed nuclei), leading to an increase up to 1000 times** (Ginges and Flambaum, 2004). The magnetic quadrupole moment also presents an enhancement due to close doublets (10 times) and collective behavior (10 times). However, there is no significant enhancement on octupole-deformed nuclei (Flambaum et al., 1997). As such, we would focus on the Schiff moment enhancement in octupole deform nuclei. It is worth noting that a similar enhancement is present for the sensitivity to a Schiff moment in polar molecules, as compared to atoms, due to the presence of nuclei with doublets of opposite parity in polar molecules (Sushkov and Flarnbaurn, 1978).

The analytical estimation of the Schiff moment in the lab frame is given by,

$$S \approx 1.0 \times 10^{-4} \frac{I}{I+1} \beta_2 \left(\beta_3\right)^2 Z A^{2/3} \frac{[\mathrm{keV}]}{E_- - E_+} e\eta \left[\mathrm{fm}^3\right] \tag{2.21}$$

where I is the nuclei spin, Z is the atomic number, A is the atomic mass ($A = Z + N$), $E_- - E_+$ is the difference in energy between two closely-lying levels with the same spin and opposite parity (doublets) mixed due to P, T-odd effects in nuclei, η is the dimensionless strength constant of the nuclear P, T-violating potential (see Spevak et al. (1997)), and β_2 and β_3 are the static nuclear quadrupole and octupole deformation, respectively (Flambaum and Dzuba, 2020).

Chapter 3

Current knowledge of RaF

3.1 Theoretical predictions of RaF

The advantages related to the use of diatomic molecules for P, T-odd violating forces have been known for more than 30 years. However, it is only until the past decade that new experiments have been able to reach the required level of precision for EDM measurements (Isaev and Berger, 2013). Most of them are based on laser cooling schemes to cool down the molecules, reducing the appearance of systematic effects and increasing the precision of the measurements. The first molecular laser-cooling results were obtained in SrF by Shuman et al. (2010), being the most sensitive measurement in the time, and starting the search for other potential candidates for laser-cooling EDM research.

Among the different molecules, RaF has gained a special interest in EDM searches. Ra is a heavy nuclei that present octupole deform isotopes with nuclear spin $I = 1/2$ (Gaffney et al., 2013), increasing its sensitivity to P, T-odd forces. Furthermore, the excitation energy of the RaF electronic states is in the visible region, making them laser accessible. Finally, it has been predicted that RaF presents a highly diagonal Franck-Condon (FC) matrix between its ground a first exited state, making it well suitable for laser-cooling methods and gaining its spotlight in parity violation experiments (Isaev et al., 2010).

The first theoretical predictions on RaF electronic levels were performed by Isaev et al. (2010). They conclude that the ground state and first exited state of the RaF are $X^2\Sigma_{1/2}$ and $A^2\Pi_{1/2}$, with an electronic transition energy of 13,300(1,200) cm^{-1}. A similar level of precision was obtained for the rest of the low-lying excited state of RaF ($B^2\Delta_{3/2}$, $B^2\Delta_{5/2}$, $A^2\Sigma_{3/2}$, $C^2\Sigma_{1/2}$), being predicted by Isaev and Berger (2013). Latter quantum chemistry calculations, including more electron correlations and quantum electrodynamics (QED) effects, have increased the precision of the electronic levels uncertainties to less than hundreds of cm^{-1} and predicted the high-lying electronic levels ($D^2\Pi_{1/2}$, $D^2\Pi_{3/2}$, $E^2\Sigma_{1/2}$, $F^2\Sigma_{1/2}$, $G^2\Pi_{1/2}$, $G^2\Pi_{3/2}$, $H^2\Sigma_{1/2}$, $I^2\Delta_{3/2}$, $I^2\Delta_{5/2}$) of RaF (Skripnikov, 2021), being critical to facilitate the search for more excited states and to perform high-resolution studies in follow-up experiments.

The most accurate predictions of RaF electronic states have been calculated following the coupled cluster (CC) numerical approach. In this approach, the molecular orbitals are described as the product of an exponential cluster operator and the usual Slater determinant of the Hartree-Fock approach, allowing the inclusion of electron correlations (Cramer, 2013). In this case, the calculations were performed using the Dirac-Coulomb Hamiltonian, correlations between 69 electrons, and the modified Gaussian-type Dyall's AEQZ basis set. The latter is defined by several functions for each atomic angular quantum number l. To increase the accu-

racy of the calculations, all the functions with $l \leq 6$ have been calculated using the relativistic Fock-space coupled-cluster calculations with single, double, and triple cluster amplitudes (FS-RCCSDT), i.e., until the third order of the cluster operator, and FS-RCCSD, i.e., until the second order, for the rest. It is worth noting that the first 18 electrons, up to 3d atomic orbital, were not included in the correlations effects as they gave a negligible contribution (Skripnikov, 2021; Athanasakis-Kaklamanakis et al., 2023).

To take into account the computational limit of a finite basis set, i.e., the physical limit to define a complete basis set (CBS), the extrapolated contribution of higher harmonics retrieved from the generalized scalar-relativistic effective core potential for 27 valence and outer core electrons has been included (CBS correction) (Skripnikov, 2021). Further improvements include the Gaunt inter-electron interaction and quantum electrodynamics (QED) effects as correction factors to the non-covariant (non-Lorentz invariant) Coulomb repulsion operator (Pernpointner, 2002). Table 3.1 shows the predicted energy of the electronic levels using purely the FS-RCCSD approach and after the inclusion of high correction factors. As can be seen, the high-lying electronic states are so close to each other that some of the uncertainties overlap (e.g., H $^2\Sigma_{1/2}$ and I $^2\Delta_{3/2}$), hindering the assignment of the experimentally measured electronic levels.

Table 3.1: RaF theoretical electronic excitation energies calculated using the FS-RCCSD approach (left), and including higher-order corrections (right). Taken from (Athanasakis-Kaklamanakis et al., 2023)

State	FS-RCCSD (cm^{-1})	Higher corrections (cm^{-1})
X $^2\Sigma_{1/2}$	0	0
A $^2\Pi_{1/2}$	13,406	13,301(26)
B $^2\Delta_{3/2}$	14,582	14,307(54)
B $^2\Delta_{5/2}$	15,403	15,103(59)
A $^2\Pi_{3/2}$	15,481	15,357(25)
C $^2\Sigma_{1/2}$	16,785	16,622(47)
D $^2\Pi_{1/2}$	22,724	22,323(116)
D $^2\Pi_{3/2}$	23,074	22,671(116)
E $^2\Sigma_{1/2}$	25,616	25,501(59)
F $^2\Sigma_{1/2}$	28,410	27,995(172)
G $^2\Pi_{1/2}$	28,962	28,797(76)
G $^2\Pi_{3/2}$	29,391	29,257(63)
H $^2\Sigma_{1/2}$	29,860	29,629(106)
I $^2\Delta_{3/2}$	29,862	29,686(70)
I $^2\Delta_{5/2}$	30,006	29,824(72)

3.2 RaF experimental data

The first measured electronic levels of RaF were retrieved in 2018 on the collinear resonance ionization spectroscopy (CRIS) set-up (Garcia Ruiz et al., 2020), being the first short half-life radioactive molecule to be studied. In this experiment, four of the low-lying excited states of RaF were measured, retrieving most of the predicted levels. However, due to the big theoretical uncertainties of these levels, one of them ($B^2\Delta_{3/2}$) was only tentative assigned. Figure 3.1 shows a schematic representation of the measured exited state on the 2018 RaF campaign.

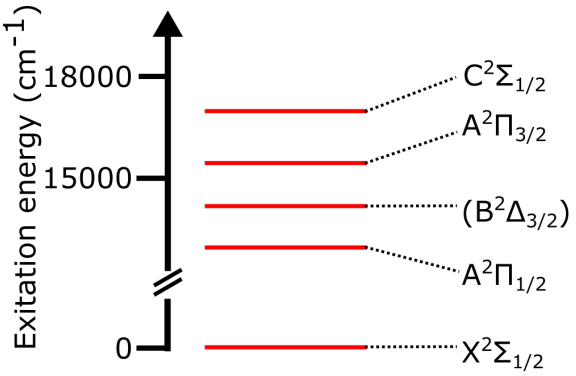

Figure 3.1: Low-lying exited state of RaF measured in the 2018 campaign (Garcia Ruiz et al., 2020).

So far, CRIS is the only experimental technique used to measure the molecular structure of RaF. This is a laser spectroscopy technique that takes advantage of a collinear geometry (high resolution) and resonant ionization schemes (high detection efficiency) to ionize the molecules and deflect them from the neutrals (high signal-to-noise ratio), producing a high-resolution spectrum with beam intensities as low as 10 to 100 ions per second (see Sect 4.2).

Currently, the most studied electronic level of RaF is its first exited state, being measured to retrieve the isotope shift across the ^{223}RaF, ^{224}RaF, ^{225}RaF, and ^{228}RaF isotopomers, exhibiting a remarkably high sensitivity to changes in Ra nuclear charge radius (Udrescu et al., 2021). Similarly, its high-resolution study has allowed the retrieval of the molecular constants of the ground and first exited state used in the present work (Udrescu et al., 2023).

Finally, based on the latest predictions on the different electronic states of RaF (see Table 3.1), most of the RaF electronic levels have been measured at CRIS during the RaF 2021 campaign at ISOLDE (See Sect 4.2). The data retrieved from this experiment has been independently studied by Athanasakis-Kaklamanakis et al. (2023) and in the present work (see Sect 5.1).

Chapter 4

Experimental setup

4.1 The ISOLDE facility

The ISOLDE Radioactive Beam Facility is one of the various buildings at CERN responsible for radioactive nuclei production (García Borge, 2016). These nuclei are produced by the collision of highly energetic protons (at 1.4 GeV) with a thick target. The wide variety of solid and liquid target materials combined with the spallation, fission, and fragmentation reactions on thick targets allows the production of radioactive isotopes covering the whole nuclear chart below uranium (García Borge, 2016). In general, the target material is kept at a high temperature (1000 to 2000^oC), allowing the diffusion of the produced exotic atoms out of the target into an adjacent ion source (Herlert, 2010). For the production of RaF, a controlled leaking valve was attached to the target to inject CF_4. CF_4 dissociates and reacts with the atoms and molecules on the target surface, forming RaF through reactive collisions. RaF molecules are ionized by a rhenium surface ion source, a metal tube of rhenium heated up to 2400^oC, allowing the ionization of the atoms with a work function lower than rhenium (Arrowsmith-Kron et al., 2023). Afterward, the RaF^+ ions are mass separated from other species using the ISOLDE's High-Resolution Separator (HRS). This consists of two bending magnets producing an electromagnetic field that deflects the ion beams according to their mass-to-charge ratio from where a beam of one particular mass A (isobars) is sent toward the experiments. The mass resolving power of the HRS is of the order of 5000 (Flanagan et al., 2013), which is sufficient to resolve isotopes with different mass A $(= Z + N)$ or molecules with mass M $(= \sum_i Z_i + N_i)$. Figure 4.1 shows a schematic representation of the production and mass separation of radioactive ion beams at ISOLDE.

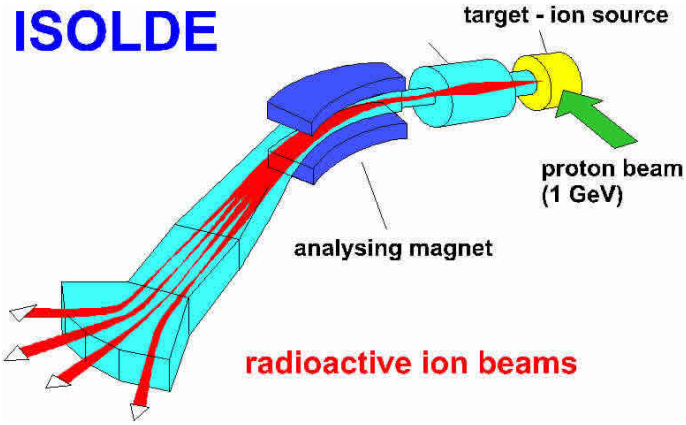

Figure 4.1: Schematic representation of the ISOL technique. Taken from (Herlert, 2010).

To reduce the kinetic energy spread, the ions are collisionally cooled to room temperature and bunched in the ISCOOL Cooler buncher, a radio-frequency quadrupole (RFQ) trap filled with helium gas (Vernon, 2020). The ions are radially confined by the RFQ potential and decelerated through several collisions with the buffer gas (helium). Furthermore, a declining DC potential with a field gradient of 0.2 V/cm drives the ions to the end of the trap, where they are accumulated by applying a trapping potential during a given time (Catherall et al., 2017). Figure 4.2 shows a schematic representation of the device operation. After ~ 20 ms of cooling and accumulation time, the DC trapping potential is turned off, and RaF^+ bunches of $5\mu s$ temporal width are released and accelerated to 40 keV before entering the collinear resonant ionization spectroscopy (CRIS) setup (Flanagan et al., 2013; Garcia Ruiz et al., 2020). By bunching the ion beam and releasing the ions in short pulses of a few microseconds, the duty cycle of the CRIS experiment is improved by several orders of magnitude because of an improved temporal overlap between the bunched ion beam and the pulsed lasers. Furthermore, the data collection can be narrowed to only when the bunches arrive at the detector, reducing the background and increasing the signal-to-noise ratio (Frånberg et al., 2008; Koszorus, 2019).

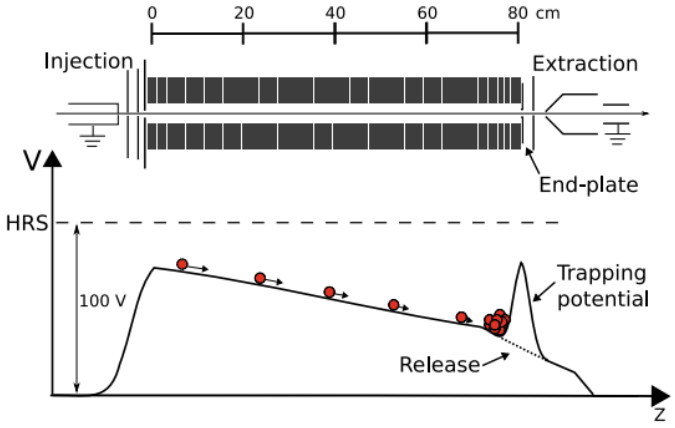

Figure 4.2: Schematic of the segmented radio frequency quadrupole trap ISCOOL (Vernon, 2020).

4.2 Collinear resonance ionization spectroscopy (CRIS)

Collinear laser spectroscopy (CLS) is based on probing an accelerated ensemble of ions or atoms with a laser overlapped collinearly to the beam direction. This technique takes advantage of the reduction in the longitudinal velocity spread through acceleration, thus, reducing the Doppler broadening and allowing the study of light elements. This can be seen in the following equation:

$$\delta E = mv\delta v \tag{4.1}$$

where m is the mass of the species of interest, δE its kinetic energy spread, v its velocity and δv its velocity spread. Since the energy spread, induced by the high temperature in the ion source, stays constant during acceleration, the velocity spread decreases as the velocity increases (Campbell et al., 2016). The reduction in the Doppler width $\nu - \nu_0$ (broadening of spectral lines) for an ion beam accelerated by a potential V_{acc} can be seen in the following equation,

$$\nu - \nu_0 = \nu_0 \frac{\delta v}{c} = \nu_0 \frac{\delta E}{c\sqrt{2eV_{acc}m}} \tag{4.2}$$

This allows collinear laser spectroscopy to reach a spectral resolution mainly defined by a combination of the linewidth of the laser and the probed state natural linewidth Campbell et al. (2016).

Collinear resonance ionization spectroscopy (CRIS) is a combined technique between CLS and resonant ionization spectroscopy (RIS). The latter is a spectroscopy technique based on the ionization of the atomic system by two or more laser-induced excitation steps (Ambartzumian and Letokhov, 1972). Due to this, CRIS possesses the Doppler-reduced conditions of a collinear experiment and the high detection efficiency and selectivity of RIS (De Groote et al., 2015). Figure 4.3 shows a schematic representation of the CRIS set-up for RaF studies.

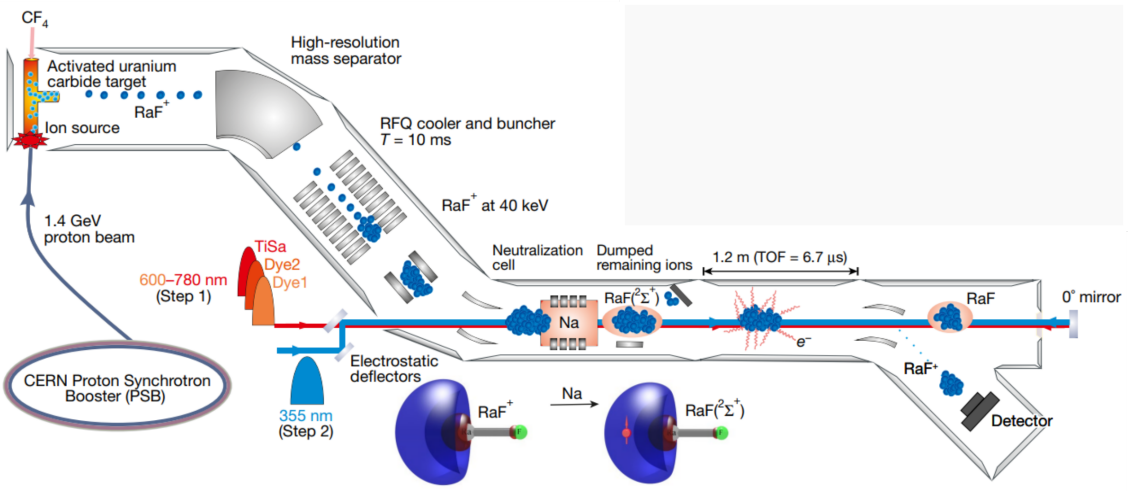

Figure 4.3: Experimental scheme for the production and study of short-lived radioactive molecules. Adapted from (Garcia Ruiz et al., 2020)

The ion bunches produced by the RFQ cooler and buncher are deflected into the CRIS beamline, where they are neutralized through a charge exchange collision with sodium vapor

in the Charge-Exchange Cell (CEC). Since the ionization energy of RaF, predicted to be around 5eV (Isaev et al., 2013), is close to that of sodium (5.14 eV), the neutralization reaction is expected to mainly populate the RaF $X^2\Sigma_{1/2}$ electronic ground state. All the non-neutralized RaF^+ ions are deflected out of the beamline axis by a deflector behind the CEC, while the neutral RaF molecules arrive at the interaction region of 1.2 m in length. This length is chosen such that it covers the spacial length of a typical ion bunch (6.7 microseconds long for a 30 keV beam). In the interaction region, the ion bunch is overlapped in time and space with several (pulsed) laser beams in a collinear arrangement (Garcia Ruiz et al., 2020).

The neutral molecules in the interaction region are ionized using a two or three-step laser scheme. In a two-step scheme, the first laser resonantly excites the molecule from the ground state to the unknown (low-lying) electronic state, scanning across the theoretically predicted energies, while the second laser non-resonantly ionizes the molecule. Similarly, to measure the high-lying electronic states, three-step laser schemes are used. In these schemes, the first laser is fixed in a know electronic state, the second laser becomes the scanning laser, and the third laser non-resonantly ionizes the molecule. Figure 4.4 shows a schematic representation of both schemes. In any of these schemes, the molecule is effectively ionized and can be manipulated with electromagnetic fields. Thus, the resonantly ionized molecules are deflected from the rest of the molecules onto a multi-channel plate (MCP) detector. The molecular excitation spectra are obtained by monitoring the ion counts as a function of the wavenumber of the scanning laser (Garcia Ruiz et al., 2020). It is worth noting that the interaction region is set in an ultra-high vacuum to ensure that the molecules are resonantly ionized and not collisionally ionized (Flanagan et al., 2013; Cocolios et al., 2013).

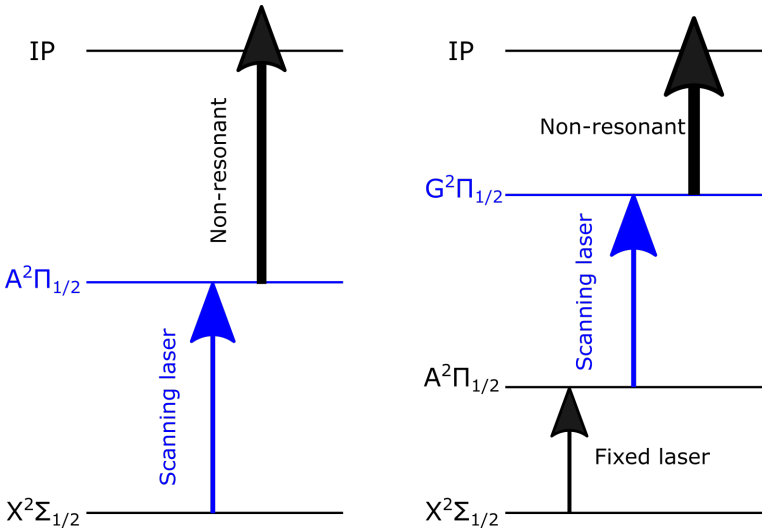

Figure 4.4: (left) Two-step ionization scheme, the first laser (blue) is used to scan the electronic level while the second non-resonantly ionizes the molecule. (right) Three-step ionization scheme, the first laser is fixed to a know electronic level, the second laser (blue) is used to scan the electronic level, and the third non-resonantly ionizes the molecule.

In the first RaF experiment (2018), none of the electronic levels of RaF were known. Furthermore, the theoretical predictions had uncertainties of around $1,200$ cm^{-1}, leading to a scanning spectral range between 12,800 cm^{-1} to 16,600 cm^{-1}. Since a typical laser linewidth is $< 0.3 cm^{-1}$, the measuring time was reduced by scanning simultaneously with three different broadband lasers that covered the complete range. Once an electronic level

was found, its transition energy was determined by blocking two of the three lasers. The lasers implemented were a pulse dye-laser system (Dye1; Spectrolase 4000, Spectron) with a linewidth of 9 GHz (0.3 cm^{-1}), a pulse dye laser (Dye2; Cobra, Sirah) with a narrower linewidth of 2.5 GHz (0.083 cm^{-1}), and a grating Ti:Sapphire (Ti:Sa) laser system with a linewidth of 2 GHz (0.067 cm^{-1}). The non-resonant transition was obtained by the third-harmonic output (355-nm) of a high-power Nd:YAG laser (TRLi 250-100, Litron) (Garcia Ruiz et al., 2020).

For the 2021 RaF campaign, the low-lying exited states were remeasured with a similar two step-scheme using a pulse dye laser with a linewidth of 9 GHz (0.3 cm^{-1}) and a non-resonant transition by the third-harmonic output (355-nm) of the Nd:YAG laser. Contrarily, the high-lying states were studied using three-step laser schemes, where the first step was obtained using a grating-based Ti:Sa fixed at 752-nm ($13,285$ cm^{-1}), corresponding to the transition between the ground state (X $^2\Sigma_{1/2}$) and the first electronic excited state (A $^2\Pi_{1/2}$) of RaF (known from the previous campaign), and the third step was a non-resonant ionization given by the second-harmonic output (532-nm) of the Nd:YAG laser. The excited state (second step) was scanned using a broadband grating-based Ti:Sa laser or a pulsed dye laser (Athanasakis-Kaklamanakis et al., 2023).

Figure 4.5 shows one of the resonant ionization schemes used in CRIS for the 2021 RaF campaign. As it can be seen, in a resonant excitation between two electronic levels, the energy of the laser has to match the difference in energy between the two electronic levels and the contribution given by the vibrational ($\Delta E_v \sim 500$ cm^{-1}) and rotational ($\Delta E_v \sim 1$ cm^{-1}) levels. As such, by scanning the second excitation step over < 100 cm^{-1} a rotational vibrational spectra between different rotational levels belonging to two vibrational levels (e.g., $\nu = 0$ and $\nu = 0$) of different electronics levels (e.g., A $^2\Pi_{1/2}$ and E $^2\Sigma_{1/2}$) can be obtained.

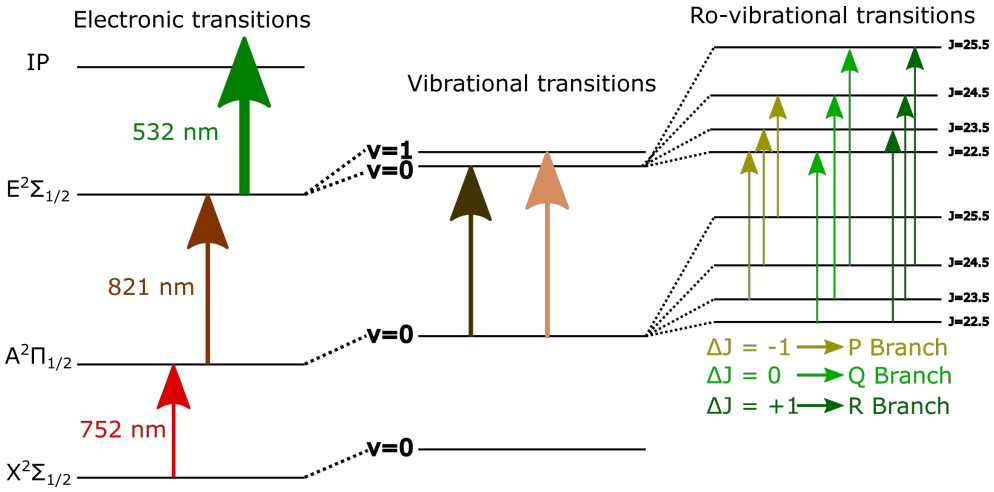

Figure 4.5: Schematic representation for a three step resonant ionization laser scheme for spectroscopy experiments of RaF at CRIS.

Figure 4.6 shows an example spectrum of the E $^2\Sigma_{1/2} \leftarrow$ A $^2\Pi_{1/2}$ transition. Since the linewidth of the laser used for scanning the different electronic states was 0.3 cm^{-1}, and the separation between rotational levels increases with J, the rotational structure ($0.05 cm^{-1} < \Delta E_J < 2 cm^{-1}$) is not well resolved for low J levels ($\sim J < 18$). The rotational peaks that can be more resolved, e.g., on the right side of the figure, belongs to transitions between high-lying rotational levels ($\sim J > 18$).

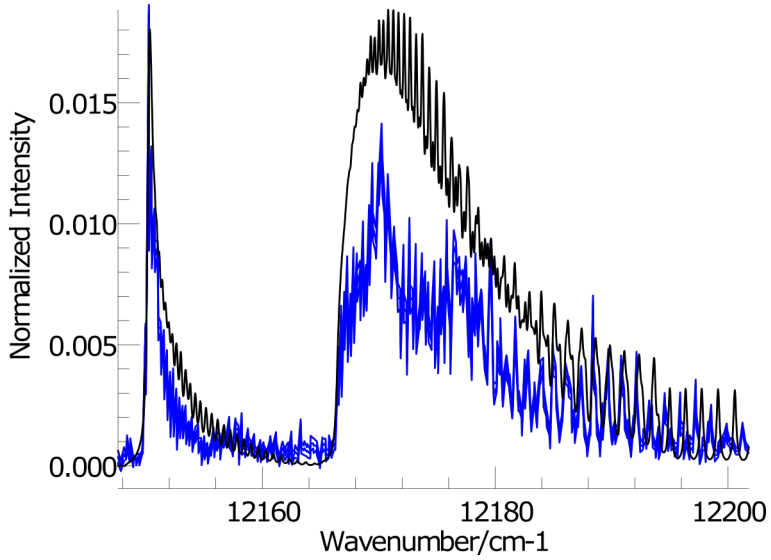

Figure 4.6: Rotational-vibrational spectrum of the E $^2\Sigma_{1/2} \leftarrow$ A $^2\Pi_{1/2}$ transition.

4.3 Linewidth broadening

The spectral lines in absorption or emission spectra are never strictly monochromatic. Due to the uncertainty principle, any energy state has a natural linewidth inversely proportional to its lifetime ($\Delta E \Delta t \sim h$). Thus, any transition will have a spectral distribution ($I[\nu_0]$) around the central frequency ν_0. The spectral distribution is defined as the line profile, while the frequency interval $\delta\nu = |\nu_2 - \nu_1|$ at the full-width at half maximum (FWHM) will give the spectral distribution resolution Demtröder (2014). The different effects that can cause spectral broadening can be classified by their nature as Gaussian or Lorentzian broadening. However, in experimental situations, several effects will be acting simultaneously. The resulting line profile is a folding integral of the Lorentzian and Gaussian distributions known as a Voight profile (Corney, 1978). Figure 4.7 shows an example of a normalized Voigt profile.

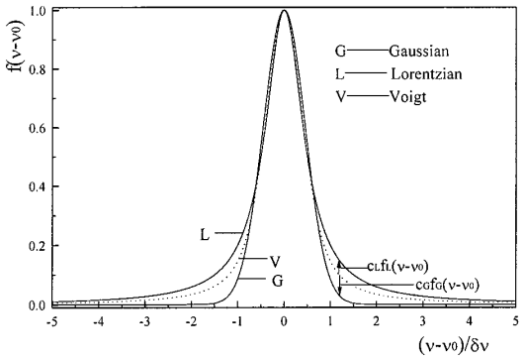

Figure 4.7: Comparison of three line profiles with the normalized intensity and the same width. Taken from Liu et al. (2001).

The molecular spectra retrieved at CRIS are given by the measurement of the laser wavelength once an ion is detected in the MCP. The latter, combined with the collinear geometry (Doppler-reduced), allows an experimental linewidth dominated by only two contributions:

the bandwidth of the laser system and a combination of natural and power broadening of the molecular levels (De Groote, 2017). Below we briefly describe all possible line-broadening effects and their magnitude for typical conditions in our experiment.

Gaussian contribution

One of the most important broadening processes in many spectroscopy studies is due to the Doppler effect, in which radiation is shifted in frequency when its source is moving towards or away from the observer. Since the molecules don't have the same velocity (Δv), the detected spectral "line" is the absorption or emission profile arising from all the resulting Doppler shifts (Atkins et al., 2014). From Eq 4.2, taking an energy spread of 4 eV and acceleration potential of 40keV, the Doppler broadening of the first exited state of RaF is $4 \cdot 10^{-4}$ cm^{-1} (10 MHz), which is negligible compared to other broadening effects.

Lorentzian contribution

An always present and unavoidable broadening effect is due to the linewidth of a given excited state, which is inversely proportional to its lifetime (τ) ($\delta E = \hbar/\tau$). Since molecular states often have a short lifetime (~ 10 ns), the associated lifetime broadening is between one and ten MHz (Hiereth, 2005). As an example, the first exited state of RaF has a lifetime lower than 50 ns ($\Delta\nu = 3$ MHz or $1 \cdot 10^{-4}$ cm^{-1}).

The electromagnetic transition stimulated by the laser field artificially shortens the lifetime of the state and leads to a broadening of the spectra. This phenomenon is called power broadening, as the broadening scales with the power of the laser implemented for the transition (Corney, 1978). In the case of a pulsed laser, the relation is more favorable than for continuous wave lasers. In a resonant ionization scheme such as CRIS, the high power of the ionization step induces a substantial power broadening which can be removed by delaying the ionization step with respect to the excitation step (decoupling them). This allows the reduction of power broadening to tens of MHz (De Groote, 2017).

Despite all the previous contributions to spectral broadening, the biggest contribution comes from the laser linewidth. Since the electronic states of RaF weren't known, the measurements were performed using lasers with linewidth from 1 to 9 GHz (0.1 to 0.3 cm^{-1}). This allowed a faster scanning time but considerably reduced the resolution of the spectra retrieved. This is also why the branches of the spectrum shown in Figure 4.6 are an envelope of all the rotational-vibrational peaks instead of separated peaks.

Chapter 5

Methodology

5.1 RaF 2021 Campaign

The electronic levels measured in the RaF 2021 campaign were based on the theoretically predicted levels given by K. Gaul, A. Kiuberis and L. Skripnikov in private communication, now submitted in (Athanasakis-Kaklamanakis et al., 2023), using a relativistic Fock-space coupled-cluster calculations with a CV4Z basis sets (Dyall, 2009, 2012), and having 27 electron correlations (27e-CV4Z). Figure 5.1 shows a schematic representation of the predicted energy levels and their associated uncertainties (σ).

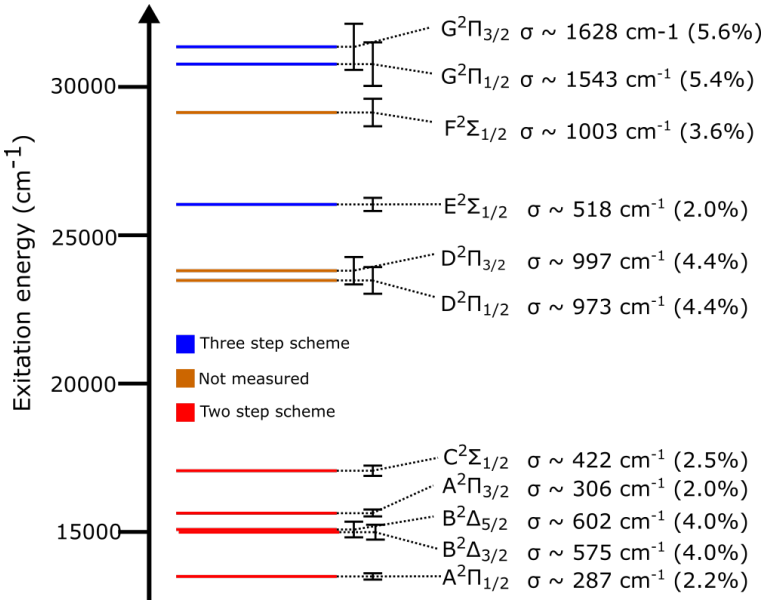

Figure 5.1: Theoretical predicted levels used for designing the laser scheme implemented on the RaF 2021 campaign. The nominal and relative uncertainty (σ) on the energy levels is given in the right side.

As it can be seen, most of the predicted levels were successfully measured, where $D^2\Pi_{1/2}$, $D^2\Pi_{3/2}$, and $F^2\Sigma_{1/2}$ were not measured due to lack of time. Furthermore, latter calculations with an improved basis set and corrections (see Sect 3.1) have shown that further energy levels ($H^2\Sigma_{1/2}$, $I^2\Delta_{3/2}$, $I^2\Delta_{5/2}$) were also measured during this campaign.

Two-step laser scheme

As aforementioned, the electronic levels of RaF were studied using two and three-step laser schemes. The first electronic excited state (A $^2\Pi_{1/2}$) has been retrieved in a two-step-scheme resonant ionization using a grating-based titanium:sapphire (Ti:Sa) laser around 752 nm ($13,285$ cm^{-1}) and non-resonantly ionized using a 355-nm Nd:YAG laser. Similarly, all the other low-lying electronic states (B$^2\Delta_{3/2}$, A$^2\Pi_{3/2}$, and C$^2\Sigma_{1/2}$) were studied using a pulsed dye laser (Pyridin 1) for the resonant excitation in the range of 14,000 and 16,700 cm^{-1}. Again, the 355-nm Nd:YAG laser was used for the non-resonant step (Athanasakis-Kaklamanakis et al., 2023). Figure 5.2 shows a schematic representation of the two-step schemes used to measure the low-lying excited states of RaF.

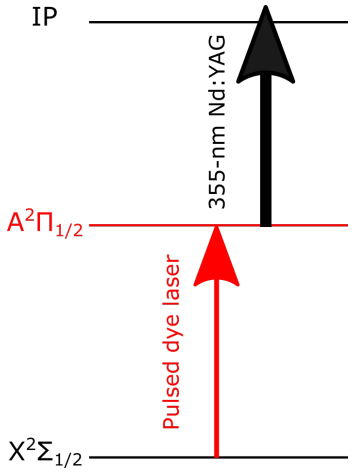

Figure 5.2: Two-step laser schemes used to scan the low-lying exited states in 2021 RaF campaign

Three-step laser scheme

The high-lying states were studied using three-step laser schemes, where the first step was obtained using a grating-based Ti:Sa fixed at $13,285$ cm^{-1} (X $^2\Sigma_{1/2} \leftarrow$ A $^2\Pi_{1/2}$), and the third step was a non-resonant ionization given by a 532-nm Nd:YAG laser. The excited state E $^2\Sigma_{1/2}$ was scanned using a grating-based Ti:Sa laser (See Figure 4.5) while all the other high-lying states were scanned using a pulsed dye laser (DCM) (Athanasakis-Kaklamanakis et al., 2023).

The Ti:Sa lasers were pumped by a 532-nm Nd:YAG laser operating at 1 kHz, and their wavelength were monitored using a HighFinesse WSU-2 wavemeter. Similarly, the pulsed dye lasers were pumped by 532-nm Nd:YAG lasers operating at 50 Hz, and their wavelength was measured by a HighFinesse WS6-600 wavemeter. These frequency rates are synchronized to the ISCOOL bunch release rate to ensure that the laser beams and the atom bunches are overlapped in space and time (De Groote, 2017). Figure 5.3 shows a schematic representation of the three-step schemes used to measure the high-lying excited state of RaF.

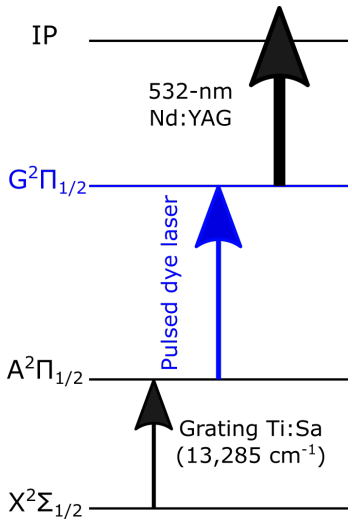

Figure 5.3: Three-step laser schemes used to scan the high-lying exited states in 2021 RaF campaign

5.2 Implemented Hamiltonian

PGOPHER, a program that calculates rotational, vibrational, and electronic spectra (Western, 2017), has been used to fit the rotational-vibrational spectra retrieved at CRIS. This program is based on the Hamiltonian presented in Section 2.2 which contains 11 main components. Table 5.1 summarizes all these components and in which cases they contribute.

Table 5.1: Components of the Hamiltonian used by PGOPHER to fit linear molecules.

Contribution for	Type of component
All molecules	Rotational
$S > 0$	Spin-Rotation
$S > 1$	Spin-Rotation
$\Lambda > 0$, $S > 0$	Spin-Orbit
$\Lambda > 0$, $S > 1$	Spin-Orbit
$S > 1/2$	Spin-Spin
$S > 3/2$	Spin-Spin
Π states	Λ doubling
Π states, $S > 0$	Λ doubling
Π states, $S > 1/2$	Λ doubling
Δ	Λ doubling

Since the current project is centered around RaF, some of the different terms present in Table 5.1 can be removed before entering the many different energy levels that compose RaF in detail. RaF is a molecule composed of only one valence electron. As such, the total electronic spin angular momentum of any electronic level is $S = 1/2$. This vanishes any spin-spin interaction and reduces the 11 components to six different components shown in Table 5.2, where the last three only contribute to Π and Δ states.

Table 5.2: Simplified components of the Hamiltonian used by PGOPHER to fit RaF.

Contribution for	Type of component
All molecules	Rotational
$S > 0$	Spin-Rotation
$\Lambda > 0$, $S > 0$	Spin-Orbit
Π states	Λ doubling
Π states, $S > 0$	Λ doubling
Δ	Λ doubling

The spectra fitting performed in PGOPHER implies the modification of all the different parameters that describe the structure of the initial and final state of the transition considered in the spectrum. However, the ground state of RaF ($X\ ^2\Sigma_{1/2}$), as well as the first exited state ($A\ ^2\Pi_{1/2}$) has already been studied in the previous years using high-resolution spectroscopy. As such, the spectra fitting performed in the current thesis takes the values of these levels as known for the spectra analysis that has them as the initial level (the ground state for two-step schemes and the first exited state for three-step schemes). This considerably reduces the complexity of the different fitting performed in the current thesis. The molecular parameters obtained by Udrescu et al. (2023), using the same CRIS setup but with a narrow band laser (17 MHz) for the scanned level, are shown in Table 5.3.

Table 5.3: Fitted rotational parameters. In the first column list the different parameters. The second and third column show the values associated to the ground ($\nu = 0$) and first exited ($\nu = 0$) state of RaF. In brackets it is shown the 1σ uncertainty. Taken from (Udrescu et al., 2023).

Parameter	$X\ ^2\Sigma_{1/2}$ (cm^{-1})	$A\ ^2\Pi_{1/2}$ (cm^{-1})
Rotational constant (B)	0.191985(10)	0.191015(10)
Centrifugal distortion constant ($10^7 \cdot D$)	1.32(10)	1.31(10)
Spin-rotation coupling constant (γ)	0.00585(10)	-
Λ-doubling constant (p)	-	-0.41071(10)
Centrifugal distortion of p ($10^7 \cdot p_D$)	-	1.9(6)
Excitation energy	-	13284.427(20)

$^2\Sigma$- and $^2\Pi$-state Hamiltonian

Since $^2\Sigma_{1/2}$ electronic states have an electronic orbital angular momentum (L) equal to zero, its projection in the inter-nuclear axis system (Λ) is also zero. Furthermore, since this is not a Π state (nor Δ), this is not double degenerate. Thus, based on Table 5.2, the only terms that contribute to the energy of this level are the rotational Hamiltonian (H_{rot}) and the spin-rotational Hamiltonian (H_{sr}). As such, the effective Hamiltonian implemented for the Σ-states of RaF (Hund's case b) was,

$$H_\Sigma = H_{rot} + H_{sr} = \left(B - D\boldsymbol{N}^2\right)\boldsymbol{N}^2 + \gamma \boldsymbol{N}\cdot\boldsymbol{S} \tag{5.1}$$

As aforementioned in Section 2.2, the rotational contribution is described as a power series where the leading constants are the rotational (B) and centrifugal distortion (D) constants. On the other hand, the spin-rotation contribution is given in terms of the spin-rotational coupling constant (γ).

Similarly, based on Table 5.2, the effective Hamiltonian implemented for the Π states (Hund's case a) was,

$$H_{\Pi} = H_{rot} + H_{sr} + H_{so} + H_{\Lambda} \tag{5.2}$$

where H_{so} is the spin-orbit Hamiltonian, and H_{Λ} is the Λ-doubling contribution. The spin-orbit contribution is described as a power series where the leading constants are the Spin-orbit coupling constant (A) and centrifugal distortion (A_D) constants. However, for $^2\Pi$ states, the effect of A_D and γ are equivalent, and thus, only one of them is normally modified Veseth (1971); Brown and Watson (1977). The Λ-doubling contribution was described in terms of the Λ-doubling constant (p) and the centrifugal distortion of p (p_D). Furthermore, since the contribution of A is an increase in the energy of the state by $A/2$ for $^2\Pi$ states, and the retrieved spectra of RaF have low resolution, its value is not taken into account, and it's directly considered in the energy value. It is worth noting that a similar Hamiltonian has been implemented for the Δ states. However, the Λ-doubling contribution was not considered for the Δ-states as its contribution is considerably smaller than for Π-states, and the resolution of the spectra was not enough to distinguish its contribution.

5.3 Thermodynamic energy of a molecular ensemble

Systems in equilibrium and rotational population distribution

In systems with many degrees of freedom, statistical mechanics allows the study of the properties of all the elements present by treating them as an ensemble. As such, for an ensemble in thermal equilibrium, we can retrieve the 'average' value of an observable property by knowing the probability of finding a given state μ and its associated observable property (Binder et al., 1993). For example, for a system with a probability distribution given by the Boltzmann distribution ($e^{-\beta E_\mu}$), the energy of the ensemble is given by,

$$\langle E \rangle = \frac{1}{Z} \sum_{\mu} E_\mu e^{-\beta E_\mu} \tag{5.3}$$

where $\beta = 1/(k_B T)$, and Z is the partition function. Z represents the probability distribution of the whole ensemble, being treated as a normalization factor. For a Boltzmann distribution, the partition function is given by,

$$Z = \sum_{\mu} e^{-\beta E_\mu} \tag{5.4}$$

As aforementioned in Section 2.2, we can approximate the energy of a linear molecule as a rigid rotor, i.e., the bond length is assumed to be fixed. As such, the rotational energy levels, with rotational quantum number J (see Sect 2.2), are to first order (ignoring the centrifugal distortion) given by,

$$E(J) \approx hcBJ(J+1) \tag{5.5}$$

where B is the rotational constant, h is the plank constant, and c is the speed of light. Combining Eq 5.4 and 5.5, we can describe the rotational partition function of a linear molecule as,

$$q_{\text{rotational}} = \sum_{J} (2J+1) e^{-\beta hcBJ(J+1)} \tag{5.6}$$

where $(2J+1)$ comes from the rotational level's degeneracy. Since B is close to one in most molecules, many rotational levels are populated at room temperature ($Tk_B \gg \Delta E_B$). As such, the rotational partition function is often expressed as,

$$q_{\text{rotational}} = \frac{k_B T}{hcB} = \frac{T}{\theta_R} \tag{5.7}$$

where θ_R is the characteristic rotational temperature. The latter is a commonly used parameter to compare the energy given by the temperature to the system with the energy gap between rotational levels (Atkins et al., 2014). Table 5.4 shows some typical values of θ_R, exhibiting the typical temperature needed to have only one rotational level populated.

Table 5.4: Rotational temperatures of diatomic molecules. Adapted from (Atkins et al., 2014)

Molecule	θ_R (K)
H_2	87.6
HCl	15.2
N_2	2.88
Cl_2	0.351
HF	30.2
RaF	3.6

First spectra: $\mathbf{E}^2\Sigma_{1/2} \leftarrow \mathbf{A}^2\Pi_{1/2}$

Using the Hamiltonian described in Sect 5.2, and knowing the molecular constants of the initial state, the data fitting of any of RaF electronic excited states can be performed by changing only the molecular constants of the scanned level, e.g., for the transition E $^2\Sigma_{1/2} \leftarrow$ A $^2\Pi_{1/2}$ only the molecular constants of E $^2\Sigma_{1/2}$ (B, D, and γ) were fitted. Figure 5.4 shows the spectrum fitting performed in PGOPHER by finding the best molecular constants of E $^2\Sigma_{1/2}$.

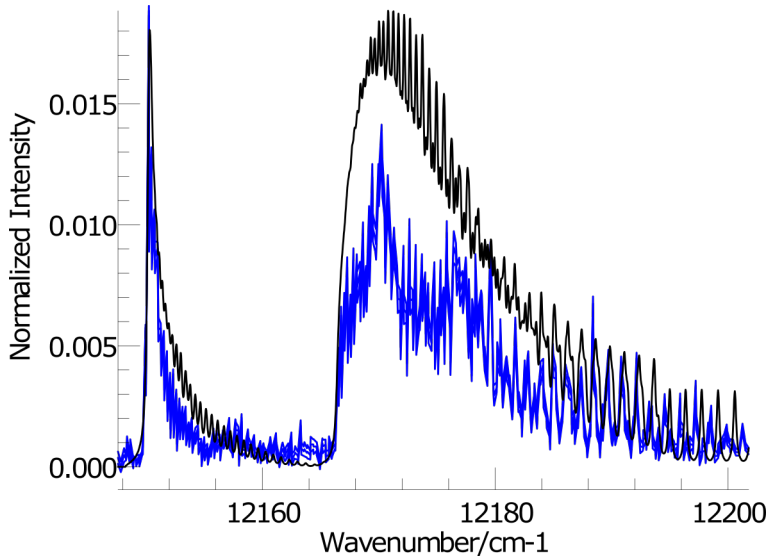

Figure 5.4: RaF E $^2\Sigma_{1/2} \leftarrow$ A $^2\Pi_{1/2}(\nu = 0 \rightarrow \nu = 0)$ transition. The blue and black curves represent the experimental and fitted spectra, respectively.

Similarly, the different high-lying excited states of RaF, measured in the second step of a three-step scheme, were fitted using only the molecular constants of the scanned level and the population distribution given by Eq 5.4.

Second spectra: $\mathbf{A}^2\Pi_{3/2} \leftarrow \mathbf{X}^2\Sigma_{1/2}$

The low-lying electronic states, scanned in the first step of a two- or three-step scheme, were fitted using the same Hamiltonian (Sect 5.2) and partition function (Eq 5.4) as in the high-lying case. However, as it can be seen in Figure 5.5, the fitted spectrum (portrait in black) is composed of two envelopes of the rotational transition, while the experimental spectrum (portrait in blue) presents nine of them. Even though the molecular constants could be changed until the fitted peaks match two experimental ones, it is impossible to match more as these constants, in this case, cannot increase the number of peaks.

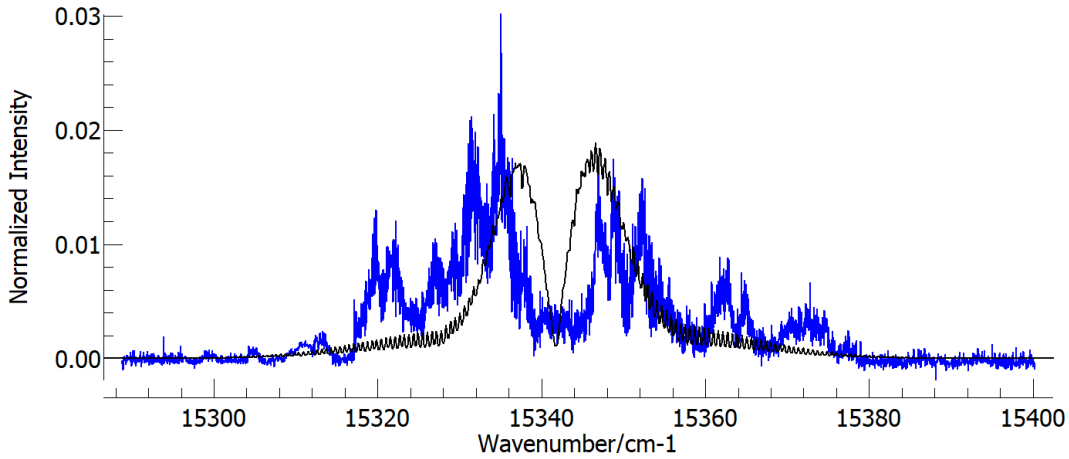

Figure 5.5: Spectra obtained from the transition A $\Pi_{3/2} \leftarrow$ X $\Sigma_{1/2}$. The blue curves represent the experimental spectra, while the black ones are the fitted ones if the observed non-uniform temperature distribution is fitted using a uniform Boltzmann distribution at room temperature.

Since the intensity of the peaks is purely dependent on the population distribution, the appearance of these extra peaks suggests a non-uniform population distribution at the ground state. This effect is not visualized on the high-lying states (see Figure 5.4), as the first step has already pre-select an ensemble of the ground state by exiting only part of the distribution. After fitting the different, first step, RaF spectra with the different population distributions suggested by PGOPHER, e.g., Boltzmann, non-Boltzmann, and Gaussian, the most accurate results were obtained using a normalized combination of Gaussian distributions given by,

$$p(J) = A_1 e^{(-b_1(J-J_{max,1})^2)} + A_2 e^{(-b_2(J-J_{max,2})^2)} + ... + A_\mu e^{(-b_\mu(J-J_{max,\mu})^2)} \tag{5.8}$$

where A_μ is a normalization constant, b_μ is the spread of the distribution, J is the rotational quantum number, and $J_{max,\mu}$ (see Eq 5.9) is the most populated rotational level of each Gaussian distribution. Figure 5.6 shows the same transition with the same molecular constants but considering three different Gaussian distributions as the population distribution of the ground state. These Gaussian distributions at different temperatures produce the appearance of extra peaks shifted by a couple of cm^{-1}. Although there is not a perfect match between the

experimental and simulated spectra ($\chi^2_{red} = 49$), the different population distributions allow more peaks to be fitted.

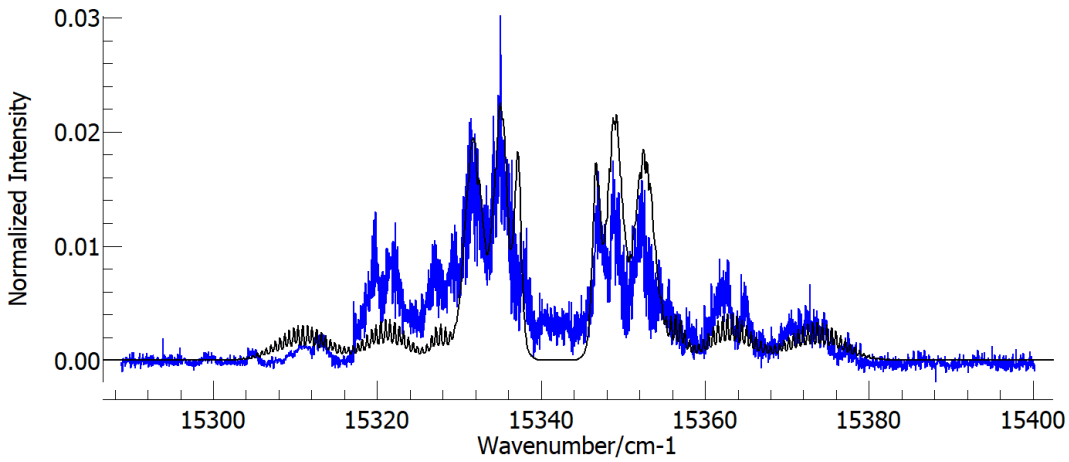

Figure 5.6: Spectra obtained from the transition A $\Pi_{3/2} \leftarrow$ X $\Sigma_{1/2}$ using three different Gaussian distributions. The blue and black curves represent the experimental and fitted spectra, respectively.

Furthermore, for a rigid rotor, we can define the rotational level with the highest population at a certain temperature T to have an angular momentum J_{max} given by,

$$J_{max} \approx \left(\frac{k_B T}{2hcB}\right)^{1/2} - \frac{1}{2} \tag{5.9}$$

Rearranging the previous equation in terms of the temperature, we can define the temperature of the distribution from the level with the highest population as,

$$T \approx \left(J_{max} + \frac{1}{2}\right)^{1/2} \frac{2hcB}{k_B} \tag{5.10}$$

This implies that, from Eq 5.10, we can retrieve the most predominant temperature in the distribution by knowing the value of J_{max} for each distribution. Like the other molecular constants (e.g., B), J_{max} is retrieved from the spectral fitting performed for each transition. It is worth noting that each electronic spectrum has been initially fitted using one distribution at room temperature, adding up to two more at higher temperatures until most of the peaks on the experimental spectra matched the simulated one. However, all the distributions were constrained to temperatures below the operating temperature of the ISOLDE ion source, as higher temperatures are not physically reachable. Furthermore, the population concentration at room temperature was prioritized, as it is expected that most of the molecules are cooled by the ISCOOL-cooler buncher.

5.4 Fitting and uncertainties

Due to the low resolution of the spectrum, the rotational structure is not fully resolved. As such, PGOPHER contour fitting tool has been implemented. This tool allows the fitting of the overall shape of an experimental spectrum to a simulated one (Western, 2017). However, this fitting only converges when the initial estimates are close to the true values. As such, an initial guess based on the molecular constants is made and improved manually with the fitting tool. Once a good agreement between the experiment and simulation has been achieved, a scan across the center values of each parameter was used to guarantee the convergence of the parameters and their associated error bars. However, low-resolution molecular spectra are multimodal problems, meaning that the same electronic spectrum can be fitted with different combinations of molecular constants. Thus, it is not guaranteed that the retrieved molecular constants are accurate. To try to overcome this problem, several simulations were run on the different scans/spectra in Python using the PGOPHER command line.

χ^2 confidence interval method

The chi-square (χ^2) is a dimensionless quantity that describes the goodness of fit and it is defined as,

$$\chi^2 = \sum_{i=1}^{k} \frac{(O_i - E_i)^2}{\sigma_i^2} \tag{5.11}$$

where O_i is the observed value, E_i is the expected value, and σ_i is the estimated standard deviations of the observed values. As such, the χ^2 is the sum of squares of the residuals weighted by the square of the experimental uncertainty (Hughes and Hase, 2010). By minimizing χ^2, it is possible to reduce the difference between the experimental and observed values, increasing the quality of the fit. Furthermore, χ^2 can be used to estimate the best-fitted parameters and their uncertainties. The latter can be estimated even for error bars that are non-uniformly distributed and for data described by non-linear functions (Hughes and Hase, 2010).

To explain the use of the χ^2 to retrieve uncertainties, let's consider the simple case of fitting a straight line to a set of points. Since χ^2 is a measure of the quality of the fit, the smaller the χ^2, the closer the fitted parameters are to the observed data trend. Thus, in the case of a straight line, the closer we are to the slope nominal value, the smaller the χ^2 will be. Furthermore, due to the definition of χ^2, its value decrease or increases quadratically as we move far away from the fitted optimal value, following a parabolic shape. This is exemplified in Figure 5.7.

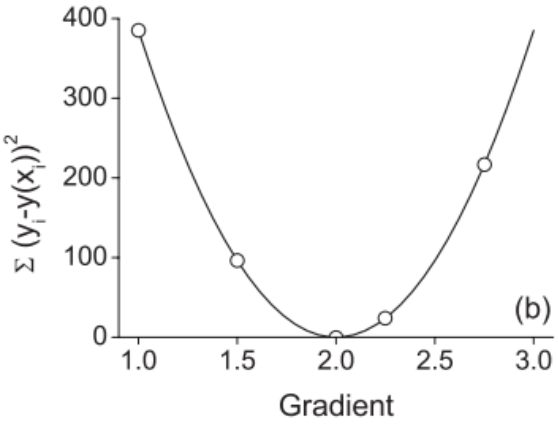

Figure 5.7: The evolution of the goodness-of fit parameter with the gradient. Taken from (Hughes and Hase, 2010).

For two different parameters, the previous figure leads to the creation of a two-dimensional surface, where the X and Y axis correspond to each parameter, and a contour or a color map represents the χ^2 values. This surface, also known as the error surface, allows the identification of model sensitivity to these parameters and their correlations. Generally, the contour around the χ^2 minimum value (χ^2_{min}) will have an elliptical shape, being the difference between the two ellipses axis an indication of the correlation between the parameters. A small difference, close to a circular shape, indicates that the uncertainties in the parameters are independent, while a more prominent elliptical shape indicates a high correlation between the two (Hughes and Hase, 2010). Figure 5.8 shows a general error surface between two fitted parameters A and B.

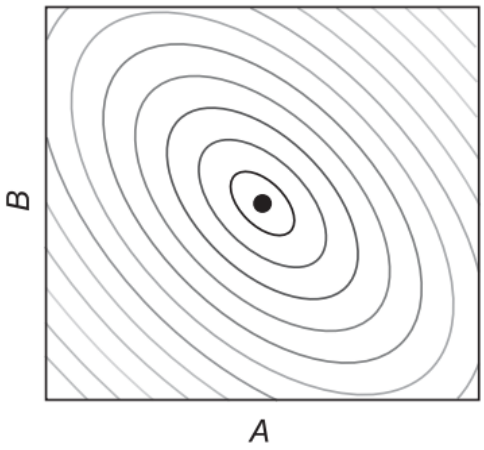

Figure 5.8: Contours of constant χ^2 in the $A - B$ plane for a general two-parameter non-linear function. The center dot represents A and B optimal values, and the contours represent an excursion equal in magnitude to the size of the error bar (Hughes and Hase, 2010).

Since χ^2 is a random variable, it has a normalized probability distribution function (PDF) given by (Squires, 2001),

$$X\left(\chi^2; v\right) = \frac{\left(\chi^2\right)^{\left(\frac{v}{2}-1\right)} \exp\left[-\chi^2/2\right]}{2^{v/2}\Gamma(v/2)} \tag{5.12}$$

where $\Gamma(x)$ is the gamma function and ν is the number of degrees of freedom. The latter is the difference between the number of points used in the fit n and the number of fitted parameters m ($\nu = n - m$). Similar to other PDFs, the probability of obtaining a value of χ^2 between χ^2_{min} and ∞ is given by the cumulative distribution function (Hughes and Hase, 2010),

$$P\left(\chi^2_{\min} \leq \chi^2 \leq \infty; v\right) = \int_{\chi^2_{\min}}^{\infty} X\left(\chi^2; v\right) \mathrm{d}\chi^2 \tag{5.13}$$

Since the probability of χ^2 changing by a certain amount ($\Delta\chi^2$) is given by the PDF, we can calculate the $\Delta\chi^2$ that corresponds to a particular confidence limit. Considering a confidence interval (CI) of 95% (2σ), that is: if the experiment is repeated many times, 95% of the time, the CI will contain the true value of the parameter (VanderPlas, 2014), we can define the CI as the region limited by,

$$\chi^2_{0.95} = \chi^2_{min} + \Delta\chi^2(\nu, 0.95) \tag{5.14}$$

where $\Delta\chi^2$ is the tabulated PDF value for a specific CI and degrees of freedom. It is worth noting that $\Delta\chi^2(\nu, 0.95)$ depends only on the number of parameters implemented in the fit and not on the goodness of fit. Thus, the CI is scaled with the square root of the reduced chi-square ($\sqrt{\chi^2_{red}}$) to account for any non-considered systematic error (Avni, 1976). By constructing this CI, we can retrieve the corresponding error bars of each parameter present in the error surface. Figure 5.9 shows an example of a CI of 68% (draw in dashed lines) for two parameters and one degree of freedom [$\Delta\chi^2(\nu = 1, 0.68) = 1$]. To retrieve the uncertainties on the parameters, we have to draw four planes tangent to the CI. One on the top, one on the bottom, and two on the sides. The difference between the value of A at which the extreme occurs and the best-fit value at χ^2_{min} ($\bar{A}$, $\bar{B}$) defines the error bar (α_a) of A. In the same way, the error bar (α_b) of B is the difference between the value of B where the extreme occurs and χ^2_{min} ($\bar{A}$, $\bar{B}$).

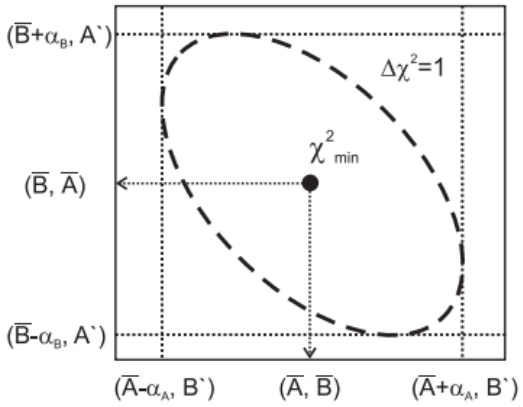

Figure 5.9: $\Delta\chi^2(\nu = 1, 0.68)$ contour for an error surface with one degree of freedom. The horizontal and vertical tangent planes define the uncertainties (α_a and α_b) in the parameters. Taken from (Hughes and Hase, 2010).

Figure 5.10 shows an example χ^2 plot between the energy and the rotational constant (B) for the E $^2\Sigma_{1/2} \leftarrow$ A $^2\Pi_{1/2}$ transition. This figure shows the high correlation (elliptical shape) between the two parameters, giving rise to possible compensation effects between molecular constants. To reduce these effects, the molecular spectra were fitted with the minimum amount of parameters possible. Furthermore, this method also allows us to prove the quality of the fit, as the plot center value should be the global minimum. If this is not the case, the fitting can be improved.

For this thesis, the different parameters that can affect the fitted spectra are the molecular constant of the initial and final state, the population distribution, and the baseline and scale of the spectrum. Thus, to take into account all the possible correlations on the uncertainties and avoid underestimation of them, all the parameters should be fitted when retrieving these error surfaces. However, the contour fitting tool can make wild changes on the molecular parameters when several parameters are not constrained unless the fit is very good (Western, 2017). Thus, some of the variables had to be constrained. Among them, the population distribution was constrained to avoid PGOPHER using temperature distributions that were not physically achievable during the experiment (below room temperature). Furthermore, since the error bars on the molecular constant of the initial state are intrinsically smaller due to the use of high-resolution spectroscopy and the availability of best-fitting tools, only the molecular constant on the final state, together with the simulation baseline and scale, were fitted for the retrieval of error bars.

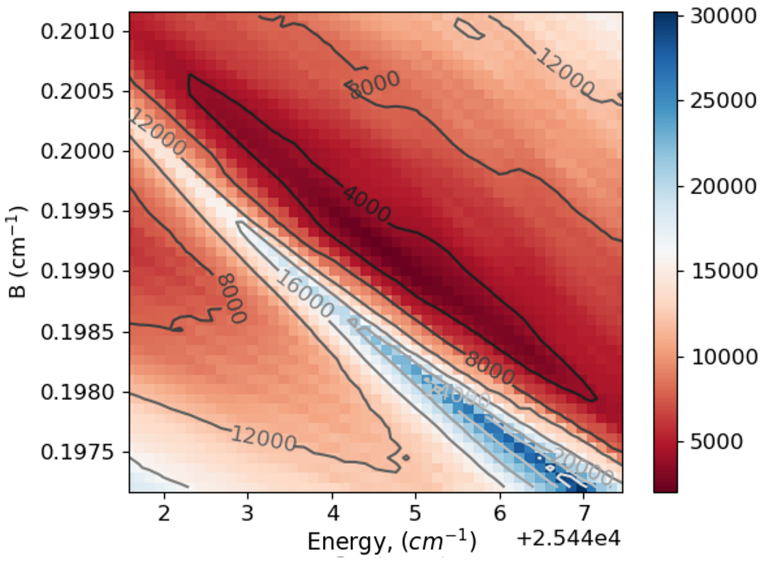

Figure 5.10: χ^2 plot between the origin and the rotational constant for the E $^2\Sigma_{1/2} \leftarrow$ A $^2\Pi_{1/2}$ transition. The elliptical shape of the contours shows the high correlation between these molecular constants.

Since retrieving the error surface can be computationally expensive, the confidence interval has been obtained for each molecular parameter at a time, having the rest of them fit. Thus, instead of having an n-dimensional error surface made out of all the parameters, a one-dimensional curve (similar to the one presented in Fig 5.7) has been obtained. Figure 5.11 shows this one dimensional χ^2 curve for the energy and the rotational constant (B) for the E

$^2\Sigma_{1/2} \leftarrow$ A $^2\Pi_{1/2}$ transition. The curve can be seen as a projection across the main axis of the ellipse present in Fig 5.10.

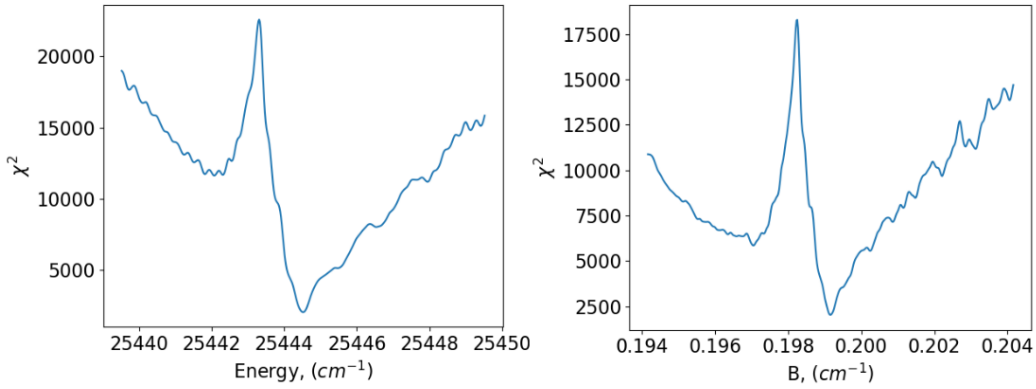

Figure 5.11: Projection of the 2D χ^2 plot on the origin and the rotational constant for the E $^2\Sigma_{1/2} \leftarrow$ A $^2\Pi_{1/2}$ transition.

The previous figure has been obtained after one fit of the floated parameters to avoid inconsistencies produced by the contour fitting tool. Thus, to perform more fitting procedures and guarantee the convergence of the simulation, it is necessary to focus on the region that contains the global minima. Figure 5.12 (left) shows the χ^2 plot until convergence (after ten-fitting procedures). As can be seen, the figure produced is not a perfect parabola, and weird effects start to appear on the curve extremes. This is mainly to the high correlation between the different parameters and the inability of the contour fitting tool to converge the model to the data. However, focusing even more on the minimum region, Figure 5.12 (right), we can see how the χ^2 curve produced follows a Gaussian-like shape in the region below the threshold for the CI (< 2350 on this spectrum). Thus, despite the problems that can arise when these constants are not optimized, the contour fitting tool allows the retrieval of the asymmetric error bars associated with each of the molecular constants.

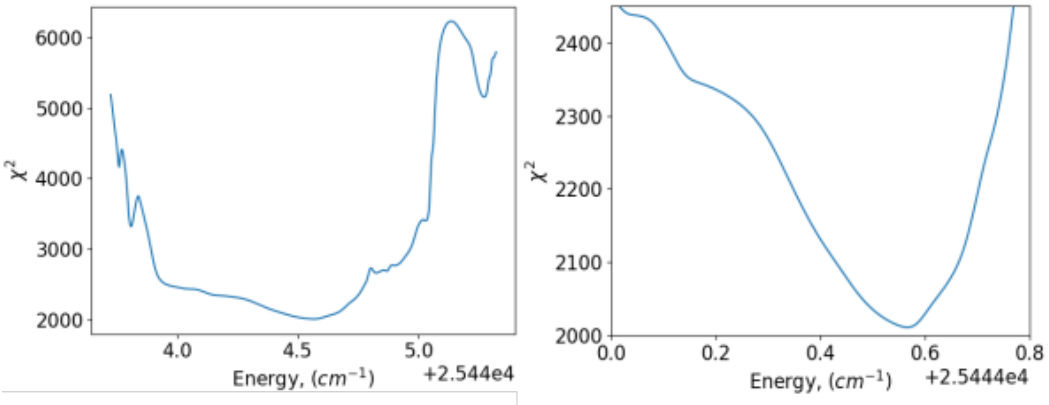

Figure 5.12: χ^2 vs energy plot after allowing PGOPHER to freely fit the parameters ten times. (left) Entire range in which the fitting was performed. (right) Zooming on the global minimum range

Chapter 6

Results

The following section presents the analysis of the data retrieved from the different measurements of the 2021 RaF campaign. First, the molecular constants of the electronic levels are retrieved. Since the low-lying electronic state presents the appearance of peaks that can be addressed as a non-uniform population distribution of the initial state, their associated concentration and internal temperatures are estimated. Finally, the data retrieved in the 2021 RaF campaign also included the measurement of different vibrational states of the same electronic state. As such, a proposed assignment of these transitions is done.

6.1 Electronic levels and molecular constants

Considering the Hamiltonian given in 5.2 and following the methodology explained in Section 5, the different molecular constants of the electronic states of RaF have been obtained. Table 6.1 shows the different molecular constants and associated correlated errors, in parenthesis, of each electronic state measured in the RaF 2021 campaign. The assignment of each spectrum to its associated electronic state has been done based on the theoretically predicted energies of RaF (see Sect 3.1).

Table 6.1: Molecular parameters retrieved using PGOPHER for the measured electronic levels of RaF. The spectra can be found on the Appendix A.1 and A.2.

Energy level	Energy (cm^{-1})	B (cm^{-1})	γ (cm^{-1})	p (cm^{-1})	D (10^{-7} cm^{-1})	χ^2_{red}
$A^2\Pi_{1/2}$	13285.0(+5/-4)	0.1908(+4/-10)	-	-0.36(+1/-4)	7(+5/-10)	16
$B^2\Delta_{3/2}$	14331.2(+1/-2)	0.1932(+3/-1)	-	-	12(±2)	72
$A^2\Pi_{3/2}$	15335.1(±4)	.1913(+2/-5)	-	-	0.2(+30/-6)	49
$C^2\Sigma_{1/2}$	16605.0(+4/-5)	0.1917(+3/-2)	0.49(+3/-2)	-	3(+1/-2)	46
$E^2\Sigma_{1/2}$	25451.1(+2/-5)	0.1991(+7/-1)	0.01(±1)	-	-9.8(+3/-2)	35
$G^2\Pi_{1/2}$	28774.1(+2/-1)	0.1999(±4)	-	-0.38(+4/-3)	-0.8(±2)	281
$G^2\Pi_{3/2}$	29262.3(+4/-3)	0.1999(+8.5/-3)	-	-	19(+2/-3)	16
$H^2\Sigma_{1/2}$	29666.2(+3/-2)	0.2006(+3/-9)	0.42(±2)	-	-	49
$I^2\Delta_{3/2}$	29693.2(+2/-4)	0.2026(+4/-5)	-	-	53(+9/-2)	130
$I^2\Delta_{5/2}$	29801.6(+2/-3)	0.2026(+2/-5)	-	-	89(+10/-6)	16

The first thing to notice is the considerable difference between rotational constants (B) across the different electronic levels. This is expected as the bond length at each electronic level can be drastically different, allowing a greater variation in the value of the rotational constant (Atkins et al., 2014). In this case, B increases with the electronic level, meaning

that the inter-atomic distance (d) between the Ra and F atom decreases ($B \propto 1/d^2$). This effect can be visualized in Fig 6.1, where the experimental spectra of the transition between the first exited state and two different high electronic states (E $^2\Sigma_{1/2}$ and H $^2\Sigma_{1/2}$) are plotted. The difference in the value of B between the initial and final state lead to a grouping of the rotational transitions called "head" (see Sect 2.3). In both of these spectra, the convergence is presented in the P branch, visualized by the small distribution in the frequency of this branch. As such, the relation between the rotational constant of the initial (B') and final state (B'') is $B'' - B' > 0$. Furthermore, B changes the distance between the P and R branches. In both of these scans, the higher the value of B, the closer these branches would be. Comparing the distance between these two experimental spectra, there is a reduction in the distance between the P and R branches from around 26 cm^{-1} (E $^2\Sigma_{1/2} \leftarrow$ A $^2\Pi_{1/2}$) to 18 cm^{-1} (H $^2\Sigma_{1/2} \leftarrow$ A $^2\Pi_{1/2}$). However, it is worth noting that this distance is also affected by the increase in the spin-rotation coupling effect (γ) in the H $^2\Sigma_{1/2}$ state.

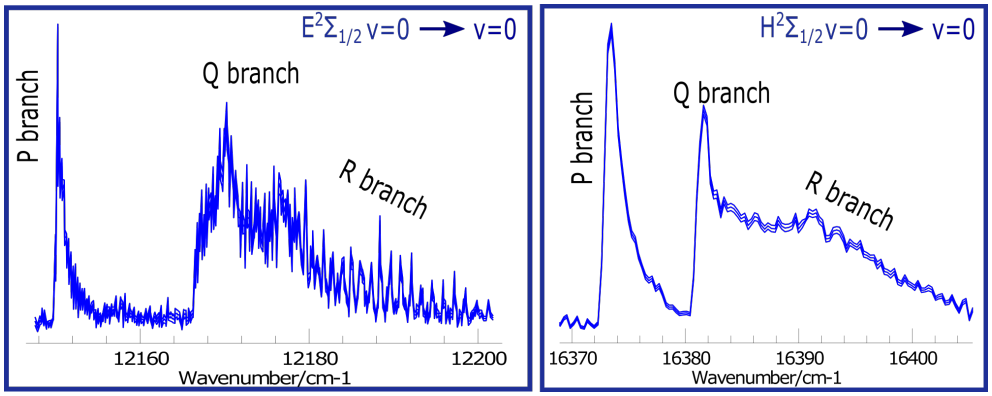

Figure 6.1: Experimental spectrum obtained in the RaF 2021 campaign (left) Rotational-vibrational spectrum of the E $^2\Sigma_{1/2} \leftarrow$ A $^2\Pi_{1/2}$ transition. (right) Rotational-vibrational spectrum of the H $^2\Sigma_{1/2} \leftarrow$ A $^2\Pi_{1/2}$ transition.

In 2.2, it was stated that for a given electronic state defined by Hund's case (a), the fine-structure electronic levels created by the spin-orbit interaction share the same B (Lefebvre-Brion and Field, 2004). As such, it is expected that the split levels of the electronic states A $^2\Pi$, G $^2\Pi$, and I $^2\Delta$ have a similar B. This has set an indirect constraint on the fitting and reduced its complexity. As it can be seen in Table 6.1, the different B agree within the error bars. It is worth noting that despite the usefulness of this constraint, each level has been initially fitted without any restriction to avoid a biased fitting.

Since D represents a correction factor of a given rotational level energy, it is the molecular constant that requires the biggest resolution to be well-defined. According to the results presented in Table 6.1, the error bar can reach values as big as its nominal value. Thus, the precision obtained with broadband spectroscopy is not good enough to well defined this constant.

As aforementioned, the molecular constants of all the electronic states of RaF have been retrieved using the molecular constants of the ground (X $^2\Sigma_{1/2}$) and first exited state (A $^2\Pi_{1/2}$) of RaF retrieved by Udrescu et al. (2023). Since the state A $^2\Pi_{1/2}$ has also been measured in a broadband approach, we can compare the value retrieved on this work with the high-resolution one. In general, the molecular constants obtained with one method and another agree within 1σ. The main difference between one and another is the inability to well

define D and that the centrifugal distortion constant of p (p_D) has not been used. Thus, despite the expected larger error bars, low-resolution spectroscopy can reliably obtain some of the molecular constants of the different electronic states of RaF.

As mentioned in Sect 2.3, the transition between one electronic state and another can also lead to a change in the vibrational state, where the relative intensities (FC factors) of different vibrational transitions between two electronic states are determined by the Franck-Condon principle. As such, assigning the vibrational state associated with the electronic state measured in a given spectrum requires the calculation of the associated FC factors for each vibrational transition. According to Isaev et al. (2010), highly diagonal FC factors (most intense transition $\Delta\nu = 0$) are expected for unpaired electrons making transitions between orbitals that do not contribute to the bonding of diatomic molecules. So far, RaF is predicted to have a highly diagonal FC factor between the ground and the first excited state. However, no other calculation of the FC factors has been made. As such, the assignment of a given spectrum as one vibrational state or another has been made purely on the intensity of the transition and the closeness to the theoretically predicted energy. Based on this criteria, the measured energies presented in Table 6.1 are considered the $\nu = 0$ vibrational state of each electronic state.

Having retrieved most of the electronic state of RaF, it is now possible to compare the accuracy of the different theories (see Sect 3.1) to the experimental ones. Figure 6.2 B) and c) shows a comparison between the most accurate theories (black labels) and the low- (red) and high-lying (blue) experimentally retrieved electronic state of RaF, respectively.

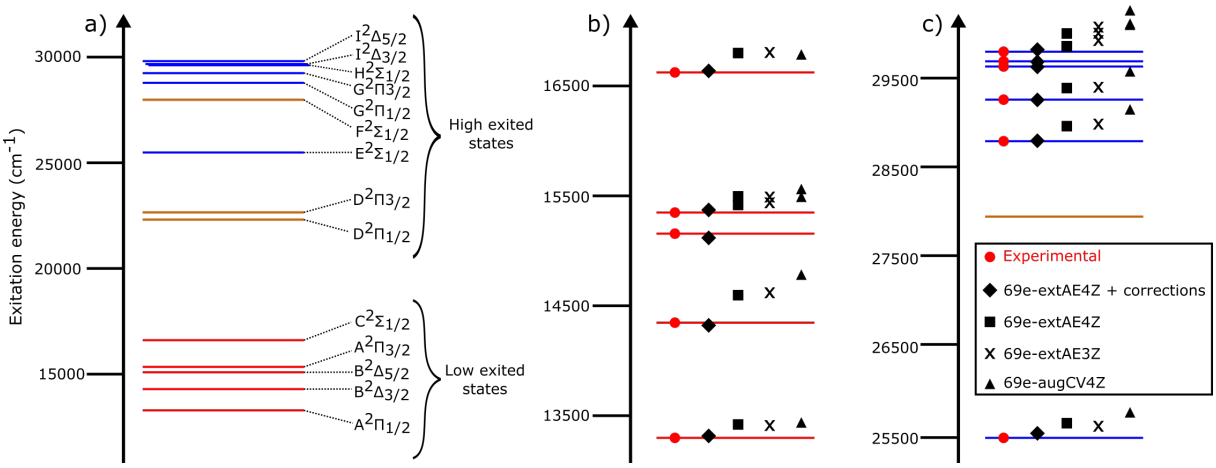

Figure 6.2: a) Schematic representation of the excited states of RaF. Orange lines are the non-measured levels of RaF. Red and blue lines represent the measured low- and high-lying excited states, respectively. b) Comparison of the excitation energy of the low-lying excited states of RaF between experimentally retrieved values and theoretical predictions. c) Comparison of the excitation energy of the high-lying excited states of RaF between experimentally retrieved values and theoretical predictions.

Compared to the initial predictions used for designing the RaF 2021 campaign (see Figure 5.1), the use of 69 electrons correlations and extended basis sets (69-ext) has considerably increased the theoretical accuracy and allowed the prediction of the $H^2\Sigma$ and $I^2\Delta$ electronic states. Furthermore, the addition of complete basis set, Gaunt inter-electron interaction,

and quantum electrodynamics corrections (69-extAE4Z + corrections) have increased the agreement between theory and experiment to at least 99.7%. Table 6.2 shows a comparison between the experimental and the current best theoretical energy of RaF electronic states.

Table 6.2: Comparison between the theoretical and experimental energy of RaF electronic states. The relative error has been calculated as $|E_{\text{exp}} - E_{\text{th}}|/E_{\text{th}}$.

State	Experimental energy (cm $^{-}$1)	Theoretical energy (cm $^{-}$1)	Relative error (%)
X $^2\Sigma_{1/2}$	0	0	-
A $^2\Pi_{1/2}$	13285.0(+5/-4)	13301(26)	0.12%
B $^2\Delta_{3/2}$	14331.2(+1/-2)	14307(54)	0.17%
A $^2\Pi_{3/2}$	15335.1(±4)	15357(25)	0.14%
C $^2\Sigma_{1/2}$	16605.0(+4/-5)	16622(47)	0.12%
E $^2\Sigma_{1/2}$	25451.1(+2/-5)	25501(59)	0.20%
G $^2\Pi_{1/2}$	28774.1(+2/-1)	28797(76)	0.08%
G $^2\Pi_{3/2}$	29262.3(+4/-3)	29257(63)	0.02%
H $^2\Sigma_{1/2}$	29666.2(+3/-2)	29629(106)	0.13%
I $^2\Delta_{3/2}$	29693.2(+2/-4)	29686(70)	0.02%
I $^2\Delta_{5/2}$	29801.6(+2/-3)	29824(72)	0.08%

6.2 Temperature distribution from RaF spectra

As aforementioned in Sect 5.3, the electronic state spectra measured in the first step of any resonant ionization scheme probes the population distribution delivered by ISCOOL. As such, the appearance of extra peaks is possible if the molecules arrive at different temperatures (population distributions). Figure 5.5 shows the B $\Delta_{3/2} \leftarrow$ X $\Sigma_{1/2}$ transition considering three Gaussian's distribution characterized by their normalized population concentration and internal temperature. Extra peaks are not present in spectra retrieved from a second step as the laser probes a pre-selected ensemble exited on the first step.

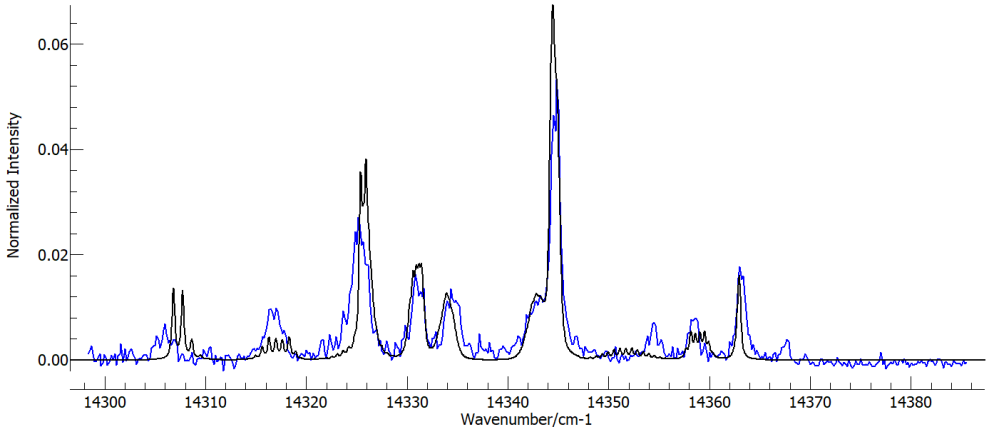

Figure 6.3: RaF B $^2\Delta_{3/2} \leftarrow$ X $^2\Sigma_{1/2}$ ($\nu = 0 \leftarrow \nu = 0$) transition (measured on 08/12/2021). The blue and black curves represent the experimental and fitted spectra, respectively.

The addition of these population concentration and associated temperatures have been made based on the peaks present in the spectrum. However, its selection can be seen as

arbitrary since the molecular constant can affect the position of these peaks. As such, a χ^2 confidence interval (See Sect 5.4), fitting the different molecular parameters, has been obtained. Furthermore, since relative changes in the Gaussian distribution centroids (J_{center}) have a lower effect than changes in the molecular constants, it was possible to retrieve the J_{center} and Gaussian concentrations (A_μ) including the correlation with the other J_{center}. That is, fitting the exited state molecular constants, and the population distribution temperatures at the same time. Figure 6.4 shows the χ^2 plots (after convergence) obtained for a Gaussian distribution above room temperature ($J_{center} = 35.5$) for the B $\Delta_{3/2} \leftarrow$ X $\Sigma_{1/2}$ transition (measured on 08/12/2021).

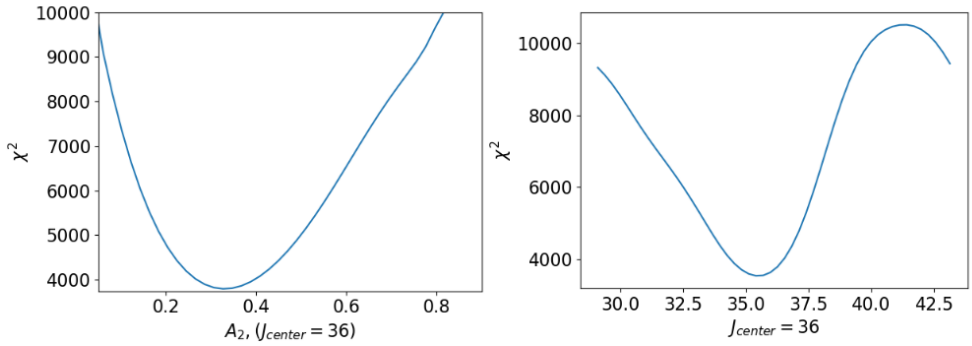

Figure 6.4: χ^2 plots used to retrieve the uncertainty in the Gaussian distribution concentration (left), and temperature (right) for the the transition B $\Delta_{3/2} \leftarrow$ X $\Sigma_{1/2}$.

Since A_μ are normalization factors, Figure 6.4 (left) has been obtained by adding or subtracting equal amounts of molecular concentrations on the other Gaussian distributions to maintain this normalization. This procedure has been implemented in RaF electronic states measured in the first step of the ionization scheme. Table 6.3 shows all the Gaussian concentrations and associated J_{center} of each Gaussian distribution used for retrieving the molecular constants of their associated spectrum. This table also includes a spectrum measured in the second step of the ionization scheme as a reference (19/11/2021).

Table 6.3: Gaussian population distribution centroids and concentration (normalized to one) measured on the first step on the listed day. The second measurement on 19/11/2021 is given as a reference for an electronic state measured in the second step of the ionization scheme.

Day measured	J_{center} distribution	A_μ Concentration
18/11/2021	22.5(+3/-5), 40.5(±3)	0.55(+10/-6), 0.45(±8)
19/11/2021	22.5(+2/-1), 35.5(+2/-1), 53.5(±2)	0.50(+14/-18), 0.35(+10/-8), 0.15(+10/-4)
19/11/2021	22.5	1
03/12/2021	22.5 (±2), 38.5 (±1), 43.5 (±1)	0.60(+6/-5), 0.30(±7), 0.10(±4)
08/12/2021	22.5(±3), 36.5(±1), 48.5(±1)	0.35(+10/-14), 0.35(+12/-10), 0.30(+12/-10)

Once the different centroids and concentrations have been obtained, the temperature of each distribution and the overall ensemble can be retrieved using Eq 5.10. The average internal temperature of each spectrum depends on the rotational constant of the electronic state (B) and the A_μ and J_{center} of each Gaussian distribution (See Eq 5.10). However, since an error

of $1E^{-3}$ on B increases the temperature error by less than 0.1 K, the current precision of the experiment makes its effect negligible.

Table 6.4 shows the calculated temperatures of the spectra measured in the first step of the ionization scheme and the day of measurement. The first thing to consider is the time of the different measurements. As can be seen, two of these measurements were taken on continuous days (18 and 19 of November). Since the retrieved temperature of these days agrees within the error bar, there is no major change in the population distribution delivered by ISCOOL. Unfortunately, the other electronic states measured in the first step of the ionization scheme were measured days later, making it impossible to correlate the change in temperature with time. Nevertheless, since the electronic state measured on 03/12/2021 presents a similar amount of molecules at room temperature as the two previous cases (55% and 50%), it seems that ISCOOL has an overall cooling capability to room temperature of around 55%. Thus, despite the non-uniform cooling of ISCOOL, it is still possible to retrieve a good number of molecules cooled. The case of the measurement performed on 08/12/2021 (see Fig 6.3) is isolated in the sense that it was the last measured electronic state in the RaF 2021 campaign. Before its measurement, the bunches arriving at CRIS followed a poor ToF distribution. Thus, the ISOLDE target was cooled down, and the injection of molecules towards ISCOOL was re-tuned. This might have affected how the molecules were cooled down and produced the spread in population distribution that appears in this spectrum.

It is worth noting that despite the error bars in J_{center}, i.e., the temperature of the distribution, is small, the associated error bars in temperature are large. Furthermore, since J_{center} is a quantum number, their error bar is only physically meaningful in quantized units. As such, even if the J_{center} error would be the minimum quantize unit (± 1), the temperature error bars would be rather large (around 40 K). Furthermore, the biggest error bar in the overall temperature is the electronic state measured on 19/11/2021 and 08/12/2021. This is mainly due to the non-linear behavior of Eq 5.10 and the presence of Gaussian distributions at high temperatures ($> 1000K$), as the error bar in the multiplication between A_μ and J_{center} is proportional to its nominal value.

Table 6.4: Average internal energy measured for first-step spectra on the listed day. The second measurement on 19/11/2021 is given as a reference for an electronic state measured in the second step of the ionization scheme.

Day measured	Temperature of J_{center} (K)	A_μ Concentration	Average internal temperature (K)
18/11/2021	295(+77/-135), 932(+119/-128)	0.55(+10/-6), 0.45(±8)	582(+105/-121)
19/11/2021	302(+42/-31), 691(+64/-48), 1581(+144/-120)	0.50(+14/-18), 0.35(+10/-8), 0.15(+10/-4)	633(+185/-107)
19/11/2021	293	1	293
03/12/2021	293(+41/-49), 577(+42/-28), 823(+47/-31)	0.60(+6/-5), 0.30(±7), 0.10(±4)	526(± 79)
08/12/2021	294(±80), 745(+35/-24), 1329(+47/-62)	0.35(+8/-6), 0.35(+10/-14), 0.30(+12/-10)	763(+192/158)

From the electronic levels measured during the RaF 2021 campaign, the first exited state, A $^2\Pi_{1/2}$, was measured at two instances. First, before all the levels mentioned in Table 6.4 on 25/10/2021 during the online run (using protons impinging on the ISOLDE target), and the second time on 03/12/2021 during the offline run (no protons impinging on the target). Figure 6.5 shows the A $^2\Pi_{1/2}$ electronic state measured at both instances. Since both measurements correspond to the same spectra, they should have the same shape and energy, being differentiated by the number of counts. However, as it can be seen in Figure 6.5 (right), there are additional peaks that appear on the right side of the spectrum that are not present on Figure 6.5 (left). Since the presence of these peaks can be attributed to the population

distribution at the moment of the measurement, it is clear that the spectrum is sensitive to the population distribution of the initial state.

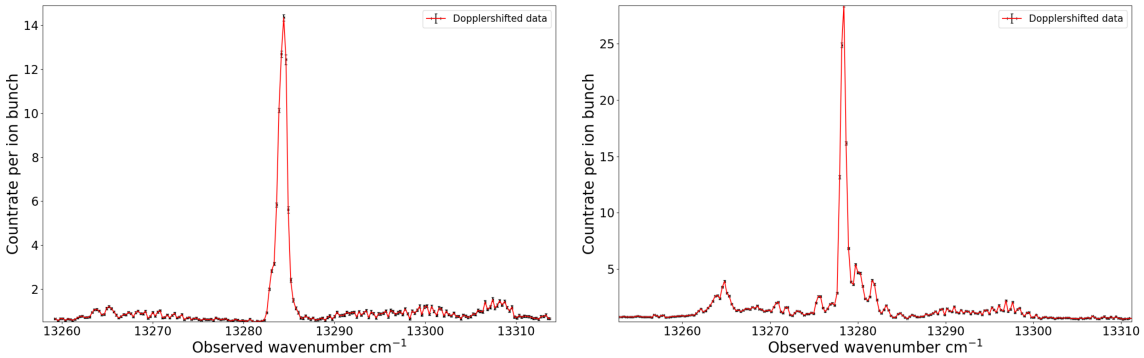

Figure 6.5: (left) A $\Pi_{1/2}$ spectrum measured at the start of the RaF 2021 campaign, and at the end (right) of the RaF 2021 campaign.

As an attempt to identify the physical reason that gives rise to these extra peaks, Figure 6.6 shows the time of flight spectra (ToF) of the bunches at the moment of the measurement of A $^2\Pi_{1/2}$. Ideally, the ToF spectra of the bunches realized by ISCOOL should follow a Gaussian distribution. However, the ToF spectrum of the online measurement 6.6 (left) is cut at the beginning of the Gaussian, meaning that ISCOOL was not properly tuned.

It is worth mentioning that there is a shift in the main peak energy between one spectrum and the other. Since the ToF of these bunches does not follow a perfect Gaussian distribution, it is possible to suffer an energy shift on the retrieved energy of the electronic state, as it has been seen in the ^{47}K hyperfine spectra (around 7.5 MHz shift) (Koszorus, 2019). As such, time cuts of the spectrum shown in Figure 6.6 (right) have been implemented to see if such an effect or any other effect appears in the retrieved spectrum. However, no energy shift was obtained, meaning that it must be smaller than the current accuracy of the scan. The only appreciable effect of these time cuts is a small relative change in the heights of the peaks, suggesting an effect on the population distribution. However, this effect is small and can be accounted for within the concentration error bars.

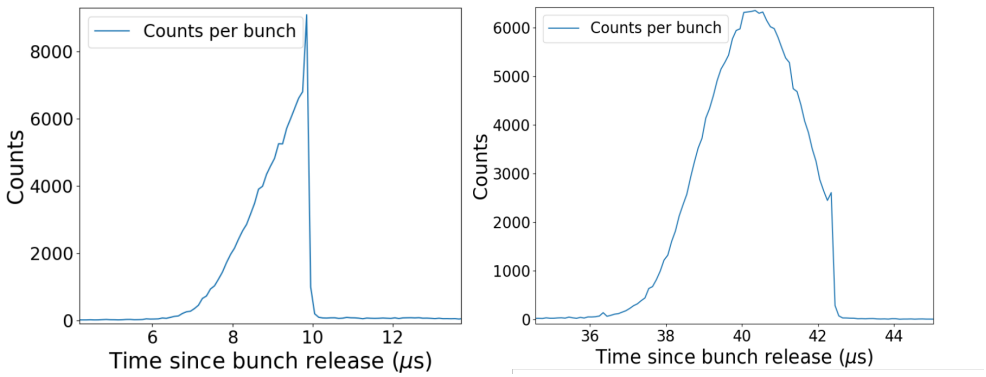

Figure 6.6: Time of flight spectra of the bunches used in the measurement of the A $\Pi_{1/2}$ state. (left) online measurement. (right) offline measurement.

As such, a distinction on the rightfulness between one spectrum and another has not been possible. However, since the energy obtained in the spectrum shown in Figure 6.5 (left) matches the values obtained by Garcia Ruiz et al. (2020), and the high-resolution study performed by Udrescu et al. (2023), this is the spectrum that was used for the retrieval of the molecular constant on the previous subsection.

6.3 Proposed assignment of higher vibrational states

Besides the $\nu = 0$ vibrational states obtained in the 2021 RaF campaign at CRIS (see Table 6.1), higher vibrational states ($\nu > 0$) have been measured. These were measured using transitions from $A^2\Pi_{1/2}(\nu = 0)$ or $A^2\Pi_{1/2}(\nu = 1)$ to a higher vibrational state of the exited state (e.g., E $^2\Sigma_{1/2}(\nu = 1)$). Table 6.5 shows the measured energies and their proposed assignment. The assignment of the electronic state for these spectra was based on the $\nu = 0$ vibrational state of the electronic states nearby, as transitions to a different vibrational state are closer than electronic ones. Furthermore, since B is weakly coupled with the vibrational state, its value would not considerably differ between $\nu = 0$ and another vibrational state. As such, the value of B was set as a constraint for fitting these transitions ($\Delta B \lesssim 1E^{-3}$). However, the high density of states and the possibility to fit some spectra as two different electronic states hinder the accuracy of the assignments. Thus, to avoid confusion, the energy levels that can be fitted as two different electronic states, at around 28787 cm^{-1} and 29754 cm^{-1}, have been highlighted in blue and red, respectively.

Table 6.5: Molecular parameters retrieved using PGOPHER for the measured RaF spectra of $\nu > 0$ vibrational states. Blue, and red rows represent a spectrum that can be fitted using two different electronic state. The spectra can be found on the Appendix A.3

Energy level	Energy (cm^{-1})	B (cm^{-1})	γ (cm^{-1})	p (cm^{-1})	D (10^{-7} cm^{-1})	χ^2_{red}
E $^2\Sigma_{1/2}(\nu = 1)$	25929.0(+2/-4)	0.1990(±1)	-0.09(+2/-1)	-	-13.5(+6/-5)	13
F $^2\Sigma_{1/2}(\nu \geq 1)$	28787.4(±1)	0.2014(±2)	0.41(±1)	-	9(±2)	66
G $^2\Pi_{1/2}(\nu = 1)$	28787.0(+3/-1)	0.1999(+4/-1)	-	-0.02(±1)	-11(+6/-4)	100
G $^2\Pi_{1/2}(\nu = 2)$	28812.1(+4/-1)	0.1999(±2)	-	-0.38(+2/-3)	19.5(±8)	70
G $^2\Pi_{1/2}(\nu = 3)$	28828.2(±1)	0.1989(+3/-1)	-	-0.37(±1)	12(+2/-3)	139
G $^2\Pi_{3/2}$	29225.9(+3/-4)	0.2004(+7/-6)	-	-	7(+7/-4)	46
H $^2\Sigma_{1/2}$	29650.4(+3/-5)	0.2006(±3)	0.42(+2/-4)	-	-	14
H $^2\Sigma_{1/2}(\nu = 2)$	29717.2(+2/-3)	0.2007(±5)	0.39(±2)	-	-	45
G $^2\Pi_{3/2}(\nu = 2)$	29750.0(±1)	0.1998(+7/-8)	-	-	18(+3/-4)	196
H $^2\Sigma_{1/2}(\nu = 3)$	29754.6(+4/-3)	0.2007(+4/-6)	0.90(±1)	-	7(±3)	138

The simplest assignment of a higher vibrational state is the $E^2\Sigma_{1/2}(\nu = 1)$ spectrum. Since the electronic state E is isolated from all the other electronic states (> 2500 cm^{-1}), the appearance of a spectrum with almost the same molecular constants nearby gives a great hint for its assignment. Since this spectrum has a higher energy than the fundamental one, with a lower intensity, and there is no other spectrum in the middle, the most probable assignment is a change in the vibrational state by one $E^2\Sigma_{1/2}(\nu = 1)$. This is because to end in a higher vibrational state, an extra amount of energy has to be given to the molecule.

Unlike the rest of the spectra, the ones found at 28787.4 cm^{-1}, 28812.1 cm^{-1}, and 28824.3 cm^{-1} were measured having as initial state $A^2\Pi_{1/2}(\nu = 1)$. As such, the fitting of the spectrum, molecular constants (see Udrescu et al. (2023)), and proposed assignments were performed accordingly.

The spectrum found around 28787.4 cm^{-1} (highlighted in light blue) is close in energy and can be fitted as the $F^2\Sigma_{1/2}$ (predicted), and $G^2\Pi_{1/2}$ states. As such, it was fitted as a $^2\Sigma_{1/2}$ and $^2\Pi_{1/2}$ state. On one hand, the fit obtained for a $^2\Pi_{1/2}$ state have similar molecular constants to $G^2\Pi_{1/2}(\nu = 0)$. On the other hand, the χ^2_{red} is better if it's fitted as a $^2\Sigma_{1/2}$ state. Nevertheless, if the spectrum corresponds to the $F^2\Sigma_{1/2}$ state, it would be a $(\nu \geq 1)$ vibrational state since it's located in a higher energy than the predicted $F^2\Sigma_{1/2}(\nu = 0)$. Similarly, if the spectrum corresponds to the $G^2\Pi_{1/2}$ state, it would be the $(\nu = 1)$ vibrational state, as the difference in energy with the $G^2\Pi_{1/2}(\nu = 0)$ is small. From the two possible assignments, $G^2\Pi_{1/2}(\nu = 1)$ is the most possible assignment for this spectrum as the difference in energy between this spectrum and the predicted $F^2\Sigma_{1/2}(\nu = 0)$ is considerably large.

The spectra found at around 28812.1 cm^{-1} and 28828.2 cm^{-1} have been fitted as $^2\Sigma_{1/2}$ and $^2\Pi_{1/2}$ states (the closest electronic states). If they are fitted as $^2\Sigma_{1/2}$ states, there is no reasonable agreement between the simulated and experimental ones. Contrary, a great agreement, in χ^2_{red} and molecular constants, was obtained for a $G^2\Pi_{1/2}$ state (the closest $^2\Pi_{1/2}$ state to these spectra). Thus, these spectra have been proposed as higher vibrational states of $G^2\Pi_{1/2}$, being $(\nu = 2)$ and $(\nu = 3)$, respectively.

The spectra found at 29225.9 cm^{-1} and 29650.4 cm^{-1}, have being fitted as $^2\Sigma_{1/2}$, $^2\Pi_{1/2}$, and $^2\Pi_{3/2}$ states. The spectrum found at 29650.4 cm^{-1} is far in energy from any $^2\Sigma_{1/2}$ states and is poorly fitted as a $^2\Pi_{1/2}$, being best fitted as a $^2\Pi_{3/2}$. Thus, it has being assigned as a $G^2\Pi_{3/2}$ state (the only $^2\Pi_{3/2}$ state nearby). However, since the energy of this spectrum is lower than the assigned $G^2\Pi_{3/2}(\nu = 0)$, and it's within the uncertainty of the predicted $G^2\Pi_{3/2}(\nu = 0)$ energy, it may correspond to the $\nu = 0$ vibrational state, while the assigned on Table 6.1 would correspond to $\nu = 1$ (assigned as $\nu = 0$ due to the bigger intensity and smaller relative error with the predicted one). Similarly, the spectrum found at 29650.4 cm^{-1} is best fitted as a $H^2\Sigma_{1/2}$ despite being lower in energy than the assigned $H^2\Sigma_{1/2}(\nu = 0)$. However, much like the previous case, its energy is within the uncertainty of the theoretical prediction, making it possible that this spectrum corresponds to the $\nu = 0$ vibrational state and the one assigned as $\nu = 0$ on Table 6.1 the $\nu = 1$.

For the spectrum found at 29717.2 cm^{-1}, the similarity of the shape to the $H^2\Sigma_{1/2}(\nu = 0)$ state, both in χ^2_{red} and molecular constants makes this the proposed assignment for the spectrum, being the $\nu = 2$ vibrational state as the spectrum is found at higher energy than $H^2\Sigma_{1/2}(\nu = 0)$.

Finally, the spectrum found at 29745.0 cm^{-1} (highlighted in light red) is one of the hardest to define. This spectrum is close enough to the $G^2\Pi$, $H^2\Sigma$, and $I^2\Delta$ states to be assigned as any of them. Based on the intensity of the spectrum, we can discard the $I^2\Delta_{5/2}$ assignment, as this spectrum is too intense to be an electronic forbidden transition (change in $\Lambda \geq 2$). Furthermore, it has not been possible to fit this spectrum as a $I^2\Delta_{3/2}$. Suggesting that this spectrum is either a $G^2\Pi$ or $H^2\Sigma$ state. This spectrum can be fitted with almost the same molecular constants as the $G^2\Pi_{3/2}(\nu = 0)$ state. However, the spectrum can also be fitted, having a better χ^2_{red}, if it fitted as a $H^2\Sigma_{1/2}$, hindering the assignment of this spectrum to one electronic state or another.

Chapter 7

Conclusions and outlook

The 2021 RaF experimental campaign at CRIS has allowed the measurement of most of the electronic state of RaF, complementing the previous study of the low-lying states of RaF performed in 2018 (Garcia Ruiz et al., 2020). Similarly to the previous campaign, the different electronic states were measured using broadband lasers to reduce the time needed to scan the different states, producing low-resolution spectra and hindering the retrieval of the molecular constants.

The low-lying electronic states of RaF have been measured using two-step resonant ionization schemes, while the high-lying electronic states were measured using three-step resonant ionization schemes. Due to this, the former has presented extra peaks due to a non-uniform population distribution of the rotational states. As such, the population distribution of the initial state for each of these spectra has been described as a linear combination of Gaussian distributions. The relative concentration and temperature of each of these distributions have been obtained, and their relative error has been estimated using the χ^2_{red} method. According to these results, most of the molecules were cooled down to room temperature, but a portion of them arrive at a higher temperature. However, the current resolution of the spectrum limits the capacity to accurately characterize this temperature, producing an error between 79 and 191 K across the different spectra. Similarly, the concentration of these Gaussian's at high temperatures is poorly known as the error bar of some of these scans can be up to 50% of its nominal value. Contrarily, the high-lying electronic states could be fitted using a single Gaussian distribution since the first excitation step has already selected a single sub-ensemble of the initial population distribution.

PGOPHER has been implemented to retrieve the molecular constants of the different electronic states of RaF. However, due to the high correlation between them, D is mostly unresolved, and the accuracy of the other molecular constants could be worse than the given uncertainties. Nevertheless, different conclusions can be derived based on the results obtained. First, the band head in the P branch across the electronic states means that the value of B for the higher electronic states is bigger than for the ground and first excited state of RaF. Furthermore, since the distance between the P and R branches on the different $^2\Sigma$ states is decreasing, the inter-nuclear distance between the two nuclei increases with the electronic states. Secondly, the energy of the electronic states is accurate as the retrieved value matches within a relative error smaller than 0.3% to the theoretical ones. Furthermore, the energy and molecular constants, except for D, obtained in the current work for the first exited state of RaF ($A^2\Pi_{1/2}$) agree with the high precision results presented by (Udrescu et al., 2023). This implies that broadband laser spectroscopy is capable to determine the energy state of RaF and

give a hint of the different molecular constants. However, since this is only one case, more energy states have to be measured in high resolution to accurately assess the feasibility of broadband laser spectroscopy for radioactive molecules.

Besides the $\nu = 0$ vibrational states of each electronic state measured during the 2021 RaF experimental campaign, higher vibrational states have also been measured. As such, a proposed assignment of them has been made based on the electronic states nearby. From them, the spectrum found at 25922.4 cm^{-1} has the most reliable assignment as the E $^2\Sigma_{1/2}$ state is isolated from the other electronic states, making E $^2\Sigma_{1/2}$ the only feasible option. Contrarily, all the other vibrational states were measured in a region with a high density of electronic states, hindering its assignment. Due to this, two of these states were double assigned (fitted as two different electronic states), as the resolution of the spectrum is not good enough to differentiate between one and the other.

With the electronic states retrieved in the present work, most of the electronic states of ^{225}RaF has been measured, leaving D$^2\Pi_{1/2}$, D$^2\Pi_{3/2}$, and F$^2\Sigma_{1/2}$ as the only non-measured electronic states of this molecule. As such, to fully retrieve the electronic structure of RaF, another experimental campaign focused on the measurement of these states should be performed. Similarly, high-resolution studies of the different electronic states of RaF have to be performed in high resolution to accurately retrieve the different molecular constants and benchmark the capacity of broadband laser spectroscopy to measure them.

Even though ^{225}Ra has been presented as a promising candidate for EDM research, other nuclei have also been theoretically studied. According to the predictions made by Flambaum and Dzuba (2020), ^{227}Ac is a more promising candidate for EDM measurements as this nucleus is predicted to present an enhancement factor of six compare to ^{225}Ra. Thus, the study of its molecular structure should be addressed. So far, only one electronic state of ^{227}AcF has already been measured during the 2022 AcF campaign at CRIS. However, it is worth noting that due to the presence of an extra valence electron (from Ac), there is an increase in complexity for the data analysis as new interactions, such as the spin-spin interaction and different electron coupling, would appear.

Bibliography

Alaee, R., Rockstuhl, C., and Fernandez-Corbaton, I. (2018). An electromagnetic multipole expansion beyond the long-wavelength approximation. *Optics Communications*, 407:17–21.

Ambartzumian, R. and Letokhov, V. (1972). Selective two-step (sts) photoionization of atoms and photodissociation of molecules by laser radiation. *Applied optics*, 11(2):354–358.

Arrowsmith-Kron, G., Athanasakis-Kaklamanakis, M., Au, M., Ballof, J., Berger, R., Borschevsky, A., Breier, A. A., Buchinger, F., Budker, D., Caldwell, L., et al. (2023). Opportunities for fundamental physics research with radioactive molecules. *arXiv preprint arXiv:2302.02165*.

Athanasakis-Kaklamanakis, M., Wilkins, S., and Au, M. (2021). Laser ionization spectroscopy of acf. Technical report.

Athanasakis-Kaklamanakis, M., Wilkins, S., Skripnikov, L., Koszorús, Á., Breier, A. A., et al. (2023). Pinning down electron correlations in raf towards searches for new physics. Under submission.

Atkins, P., Atkins, P. W., and de Paula, J. (2014). *Atkins' physical chemistry*. Oxford university press.

Auerbach, N., Flambaum, V., and Spevak, V. (1996). Collective t-and p-odd electromagnetic moments in nuclei with octupole deformations. *Physical review letters*, 76(23):4316.

Auerbach, N. and Zelevinsky, V. (2009). Nuclear structure aspects of schiff moment and search for collective enhancements. In *Rare Isotopes And Fundamental Symmetries*, pages 135–149. World Scientific.

Avni, Y. (1976). Energy spectra of x-ray clusters of galaxies. *The Astrophysical Journal*, 210:642–646.

Bethe, H. (1933). Quantenmechanik der ein-und zwei-elektronenprobleme. In *Quantentheorie*, pages 273–560. Springer.

Binder, K., Heermann, D., Roelofs, L., Mallinckrodt, A. J., and McKay, S. (1993). Monte carlo simulation in statistical physics. *Computers in Physics*, 7(2):156–157.

Brown, J. and Merer, A. (1979). Lambda-type doubling parameters for molecules in π electronic states of triplet and higher multiplicity. *Journal of Molecular Spectroscopy*, 74(3):488–494.

Brown, J. M. and Carrington, A. (2003). *Rotational spectroscopy of diatomic molecules*. Cambridge university press.

Brown, J. M. and Watson, J. K. (1977). Spin-orbit and spin-rotation coupling in doublet states of diatomic molecules. *Journal of Molecular Spectroscopy*, 65(1):65–74.

Campbell, P., Moore, I., and Pearson, M. (2016). Laser spectroscopy for nuclear structure physics. *Progress in Particle and Nuclear Physics*, 86:127–180.

Catherall, R., Andreazza, W., Breitenfeldt, M., Dorsival, A., Focker, G., Gharsa, T., Giles, T., Grenard, J., Locci, F., Martins, P., et al. (2017). The isolde facility. *Journal of Physics G: Nuclear and Particle Physics*, 44(9):094002.

Cocolios, T. E., Al Suradi, H., Billowes, J., Budinčević, I., De Groote, R., De Schepper, S., Fedosseev, V., Flanagan, K., Franchoo, S., Ruiz, R. G., et al. (2013). The collinear resonance ionization spectroscopy (cris) experimental setup at cern-isolde. *Nuclear Instruments and Methods in Physics Research Section B: Beam Interactions with Materials and Atoms*, 317:565–569.

Corney, A. (1978). *Atomic and laser spectroscopy*. Clarendon Press Oxford.

Cramer, C. J. (2013). *Essentials of computational chemistry: theories and models*. John Wiley & Sons.

De Groote, R., Budinčević, I., Billowes, J., Bissell, M., Cocolios, T. E., Farooq-Smith, G. J., Fedosseev, V., Flanagan, K., Franchoo, S., Ruiz, R. G., et al. (2015). Use of a continuous wave laser and pockels cell for sensitive high-resolution collinear resonance ionization spectroscopy. *Physical review letters*, 115(13):132501.

De Groote, R. P. (2017). *High resolution collinear resonance ionization spectroscopy of neutron-rich ^{76,77,78}Cu isotopes*. PhD thesis, KU Leuven. Presented 18 Sep 2017.

Demtröder, W. (2014). *Laser spectroscopy 1: basic principles*. Springer.

Dyall, K. G. (2009). Relativistic double-zeta, triple-zeta, and quadruple-zeta basis sets for the 4s, 5s, 6s, and 7s elements. *The Journal of Physical Chemistry A*, 113(45):12638–12644.

Dyall, K. G. (2012). Core correlating basis functions for elements 31–118. *Theoretical Chemistry Accounts*, 131:1–11.

Engel, J., Ramsey-Musolf, M. J., and Van Kolck, U. (2013). Electric dipole moments of nucleons, nuclei, and atoms: The standard model and beyond. *Progress in Particle and Nuclear Physics*, 71:21–74.

Flambaum, V. (2019). Enhanced nuclear schiff moment and time-reversal violation in th 229-containing molecules. *Physical Review C*, 99(3):035501.

Flambaum, V. and Dzuba, V. (2020). Electric dipole moments of atoms and molecules produced by enhanced nuclear schiff moments. *Physical Review A*, 101(4):042504.

Flambaum, V., Murray, D., and Orton, S. (1997). Time invariance violating nuclear electric octupole moments. *Physical Review C*, 56(5):2820.

Flanagan, K., Lynch, K., Billowes, J., Bissell, M., Budinčević, I., Cocolios, T. E., De Groote, R., De Schepper, S., Fedosseev, V., Franchoo, S., et al. (2013). Collinear resonance ionization spectroscopy of neutron-deficient francium isotopes. *Physical review letters*, 111(21):212501.

Frånberg, H., Delahaye, P., Billowes, J., Blaum, K., Catherall, R., Duval, F., Gianfrancesco, O., Giles, T., Jokinen, A., Lindroos, M., et al. (2008). Off-line commissioning of the isolde cooler. *Nuclear Instruments and Methods in Physics Research Section B: Beam Interactions with Materials and Atoms*, 266(19-20):4502–4504.

Gaffney, L. P., Butler, P. A., Scheck, M., Hayes, A. B., Wenander, F., Albers, M., Bastin, B., Bauer, C., Blazhev, A., Bönig, S., et al. (2013). Studies of pear-shaped nuclei using accelerated radioactive beams. *Nature*, 497(7448):199–204.

García Borge, M. J. (2016). Highlights of the isolde facility and the hie-isolde project. *Nuclear Instruments and Methods in Physics Research B*.

Garcia Ruiz, R. F., Berger, R., Billowes, J., Binnersley, C., Bissell, M., Breier, A., Brinson, A., Chrysalidis, K., Cocolios, T., Cooper, B., et al. (2020). Spectroscopy of short-lived radioactive molecules. *Nature*, 581(7809):396–400.

Garcia Ruiz, R. F. and Wilkins, S. (2020). Rotational and hyperfine structure of raf molecules: Garcia ruiz, rf: Massachusetts institute of technology wilkins, sg: Cern. Technical report.

Ginges, J. and Flambaum, V. V. (2004). Violations of fundamental symmetries in atoms and tests of unification theories of elementary particles. *Physics Reports*, 397(2):63–154.

Greaves, H. and Thomas, T. (2014). On the cpt theorem. *Studies in History and Philosophy of Science Part B: Studies in History and Philosophy of Modern Physics*, 45:46–65.

Haxton, W. and Henley, E. (1983). Enhanced t-nonconserving nuclear moments. *Physical Review Letters*, 51(21):1937.

Herlert, A. (2010). The isolde facility. *Nuclear Physics News*, 20(4):5–12.

Herzberg, G. and Mrozowski, S. (1951). Molecular spectra and molecular structure. i. spectra of diatomic molecules. *American Journal of Physics*, 19(6):390–391.

Hiereth, M. (2005). Quantenmechanik der ein-und zwei-elektronenprobleme. In *Molecular spectroscopy*. TU Braunschweig.

Hollas, J. M. (2004). *Modern spectroscopy*. John Wiley & Sons.

Hughes, I. and Hase, T. (2010). *Measurements and their uncertainties: a practical guide to modern error analysis*. OUP Oxford.

Isaev, T. and Berger, R. (2013). Lasercooled radium monofluoride: A molecular all-in-one probe for new physics. *arXiv preprint arXiv:1302.5682*.

Isaev, T., Hoekstra, S., and Berger, R. (2010). Laser-cooled raf as a promising candidate to measure molecular parity violation. *Physical Review A*, 82(5):052521.

Isaev, T., Hoekstra, S., Willmann, L., and Berger, R. (2013). Ion neutralisation mass-spectrometry route to radium monofluoride (raf). *arXiv preprint arXiv:1310.1511*.

Khriplovich, I. B. and Lamoreaux, S. K. (2012). *CP violation without strangeness: electric dipole moments of particles, atoms, and molecules*. Springer Science & Business Media.

Koszorus, A. (2019). *Collinear Resonance Ionization Spectroscopy of potassium isotopes: crossing N= 32*. PhD thesis, KU Leuven.

Kozlov, M. G. and Labzowsky, L. N. (1995). Parity violation effects in diatomics. *Journal of Physics B: Atomic, Molecular and Optical Physics*, 28(10):1933.

Langenberg, J. D., DaBell, R. S., Shao, L., Dreessen, D., and Morse, M. D. (1998). Resonant two-photon ionization spectroscopy of jet-cooled ruc. *The Journal of chemical physics*, 109(18):7863–7875.

Lefebvre-Brion, H. and Field, R. W. (2004). *The spectra and dynamics of diatomic molecules: revised and enlarged edition*. Elsevier.

LibreTexts (2023). Physical chemistry. *LibreTexts.[Google Scholar]*.

Liu, C.-P., Haxton, W., Ramsey-Musolf, M., Timmermans, R., and Dieperink, A. (2006). Schiff theorem and the electric dipole moments of hydrogen-like atoms. In *AIP Conference Proceedings*, volume 842, pages 775–777. American Institute of Physics.

Liu, Y., Lin, J., Huang, G., Guo, Y., and Duan, C. (2001). Simple empirical analytical approximation to the voigt profile. *JOSA B*, 18(5):666–672.

Nano, A. (2015). *Towards optical memories: switchable optical systems for electron and energy transfer processes*. PhD thesis, Université de Strasbourg.

Pernpointner, M. (2002). The effect of the gaunt interaction on the electric field gradient. *Journal of Physics B: Atomic, Molecular and Optical Physics*, 35(2):383.

Pospelov, M. and Ritz, A. (2005). Electric dipole moments as probes of new physics. *Annals of physics*, 318(1):119–169.

Purcell, E. and Ramsey, N. (1950). On the possibility of electric dipole moments for elementary particles and nuclei. *Physical Review*, 78(6):807.

Rossi, L. and Brüning, O. (2012). High luminosity large hadron collider: A description for the european strategy preparatory group. Technical report.

Safronova, M., Budker, D., DeMille, D., Kimball, D. F. J., Derevianko, A., and Clark, C. W. (2018). Search for new physics with atoms and molecules. *Reviews of Modern Physics*, 90(2):025008.

Schiff, L. (1963). Measurability of nuclear electric dipole moments. *Physical Review*, 132(5):2194.

Sen'kov, R., Auerbach, N., Flambaum, V., and Zelevinsky, V. (2007). Schiff theorem revisited. *arXiv preprint arXiv:0710.3367*.

Shuman, E. S., Barry, J. F., and DeMille, D. (2010). Laser cooling of a diatomic molecule. *Nature*, 467(7317):820–823.

Singh, A. K., Angom, D., and Natarajan, V. (2013). Observation of the nuclear magnetic octupole moment of 173 yb from precise measurements of the hyperfine structure in the 3 p 2 state. *Physical Review A*, 87(1):012512.

Skripnikov, L. V. (2021). Approaching mev level for transition energies in the radium monofluoride molecule raf and radium cation ra+ by including quantum-electrodynamics effects. *The Journal of Chemical Physics*, 154(20):201101.

Spevak, V., Auerbach, N., and Flambaum, V. (1997). Enhanced t-odd, p-odd electromagnetic moments in reflection asymmetric nuclei. *Physical Review C*, 56(3):1357.

Squires, G. L. (2001). *Practical physics*. Cambridge university press.

Sushkov, O., Flambaum, V., and Khriplovich, I. (1984). Possibility of investigating p-and t-odd nuclear forces in atomic and molecular experiments. *Zh. Eksp. Teor. Fiz*, 87:1521.

Sushkov, P. and Flarnbaurn, V. (1978). Parity breaking effects in diatomic molecules. *Zh. Eksp. Teor. Fiz*, 75:1208–1213.

Udrescu, S., Brinson, A., Ruiz, R. G., Gaul, K., Berger, R., Billowes, J., Binnersley, C., Bissell, M., Breier, A., Chrysalidis, K., et al. (2021). Isotope shifts of radium monofluoride molecules. *Physical Review Letters*, 127(3):033001.

Udrescu, S.-M., Wilkins, S., Breier, A., Ruiz, R. F. G., Athanasakis-Kaklamanakis, M., Au, M., Belošević, I., Berger, R., Bissell, M., Chrysalidis, K., et al. (2023). Precision spectroscopy and laser cooling scheme of a radium-containing molecule.

VanderPlas, J. (2014). Frequentism and bayesianism: a python-driven primer. *arXiv preprint arXiv:1411.5018*.

Vernon, A. R. (2020). *Collinear Resonance Ionization Spectroscopy of Neutron-Rich Indium Isotopes*. Springer Nature.

Veseth, L. (1971). Corrections to the spin-orbit splitting in 2π states of diatomic molecules. *Journal of Molecular Spectroscopy*, 38(2):228–242.

Western, C. M. (2017). Pgopher: A program for simulating rotational, vibrational and electronic spectra. *Journal of Quantitative Spectroscopy and Radiative Transfer*, 186:221–242.

Appendices

Appendix A

RaF electronic states spectra

The present appendix shows the spectra (blue) and fitting (black) of the different electronic states of RaF in PGOPHER.

A.1 Low-lying electronic states

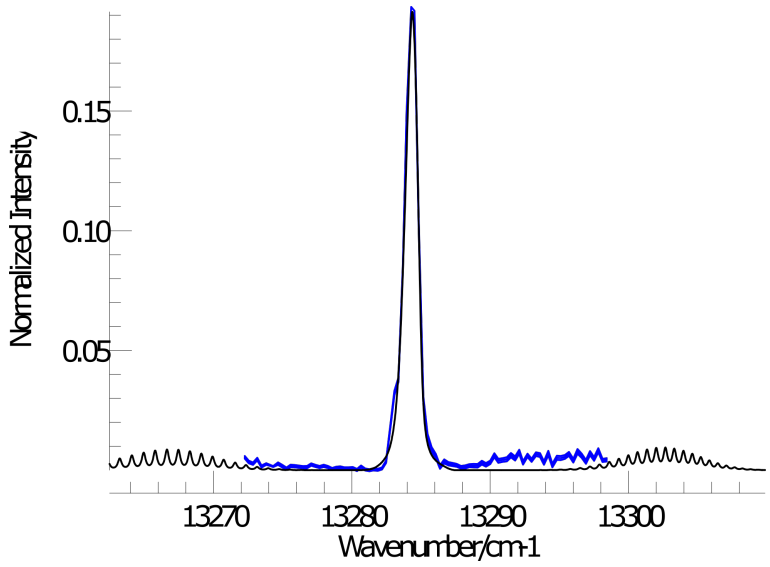

Figure A.1: Rotational-vibrational spectrum of the A $^2\Pi_{1/2} \leftarrow$ X $^2\Sigma_{1/2}$ transition.

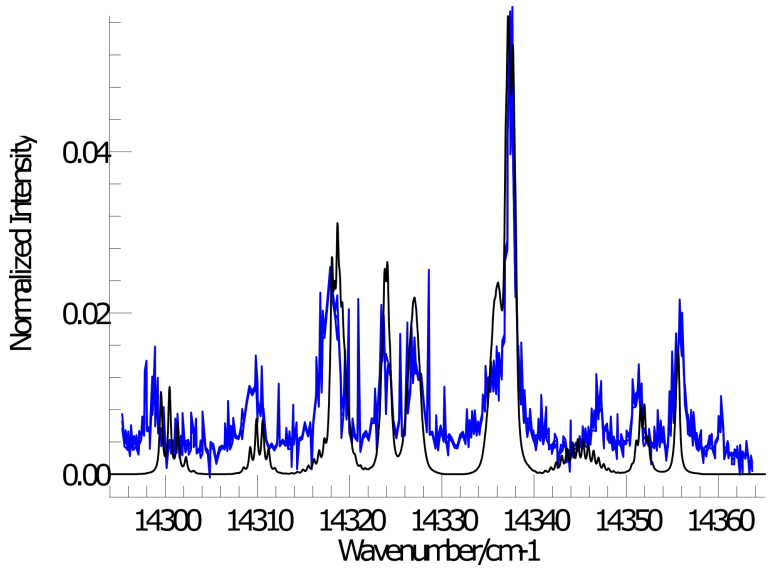

Figure A.2: Rotational-vibrational spectrum of the B $^2\Delta_{3/2} \leftarrow$ X $^2\Sigma_{1/2}$ transition.

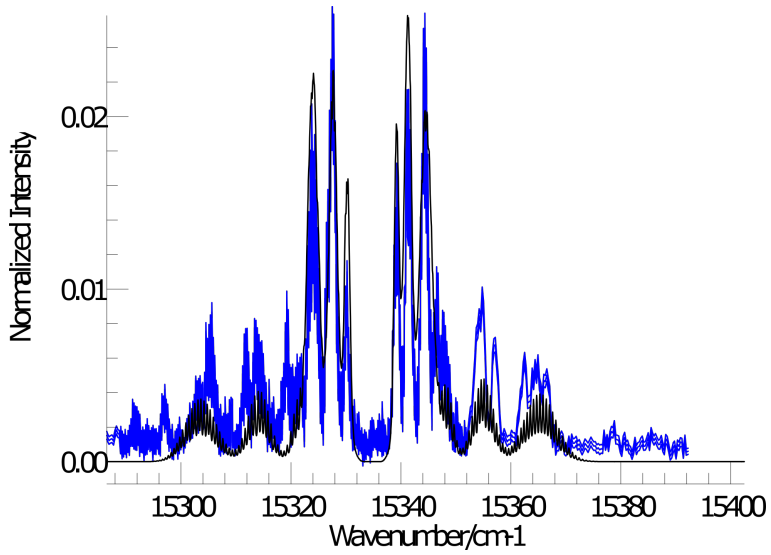

Figure A.3: Rotational-vibrational spectrum of the A $^2\Pi_{3/2} \leftarrow$ X $^2\Sigma_{1/2}$ transition.

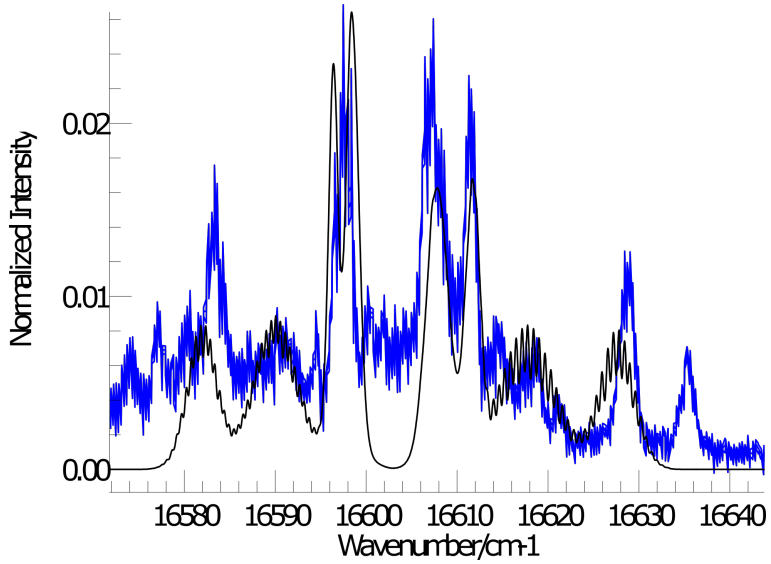

Figure A.4: Rotational-vibrational spectrum of the C $^2\Sigma_{1/2} \leftarrow$ X $^2\Sigma_{1/2}$ transition.

A.2 High-lying electronic states

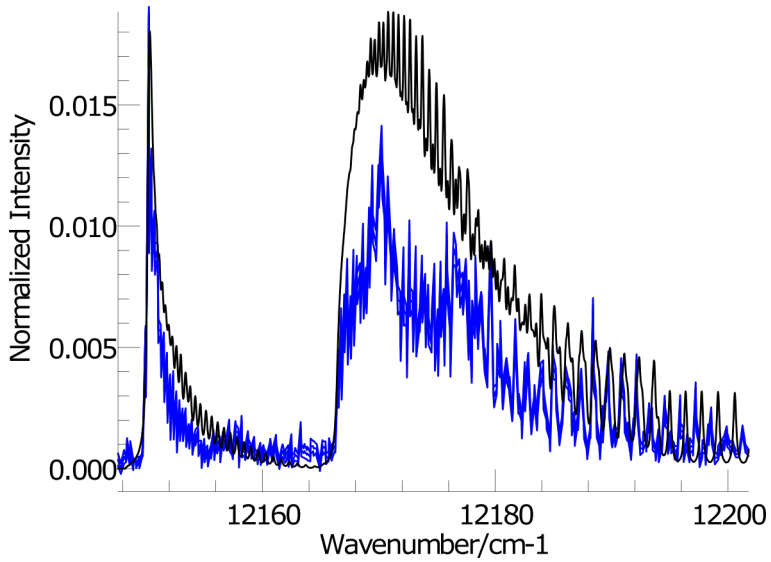

Figure A.5: Rotational-vibrational spectrum of the E $^2\Sigma_{1/2} \leftarrow$ A $^2\Pi_{1/2}$ transition.

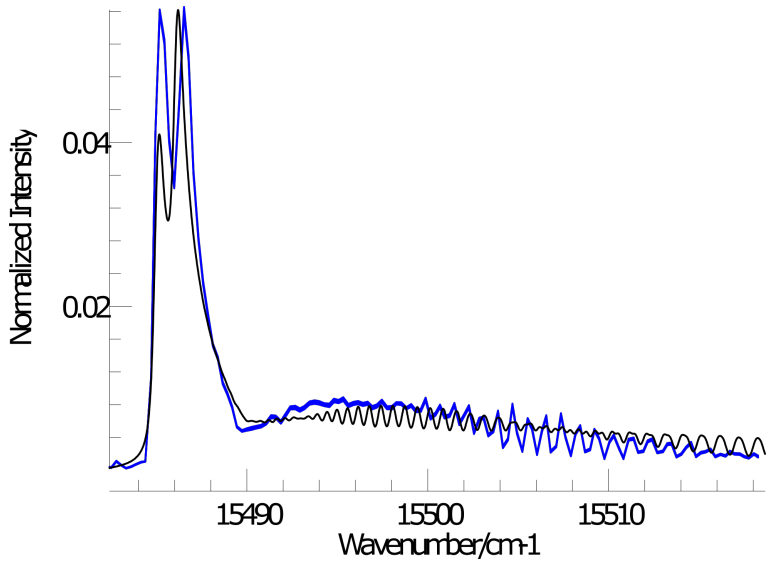

Figure A.6: Rotational-vibrational spectrum of the G $^2\Pi_{1/2} \leftarrow$ A $^2\Pi_{1/2}$ transition.

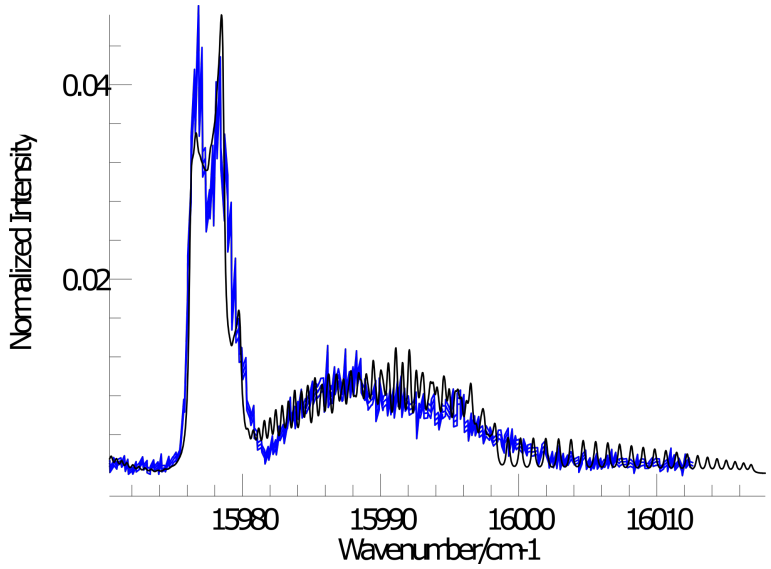

Figure A.7: Rotational-vibrational spectrum of the G $^2\Pi_{3/2} \leftarrow$ A $^2\Pi_{1/2}$ transition.

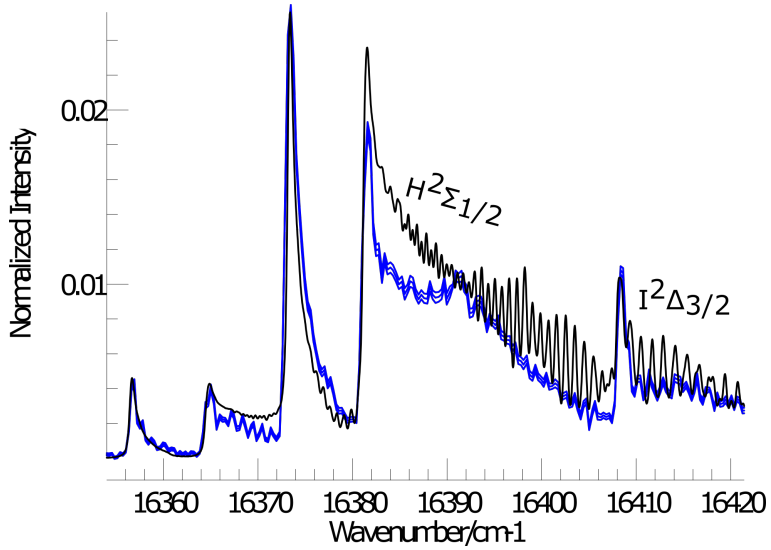

Figure A.8: Rotational-vibrational spectrum of the H $^2\Sigma_{1/2} \leftarrow$ A $^2\Pi_{1/2}$ (center) and I $^2\Delta_{3/2} \leftarrow$ A $^2\Pi_{1/2}$ (right) transitions.

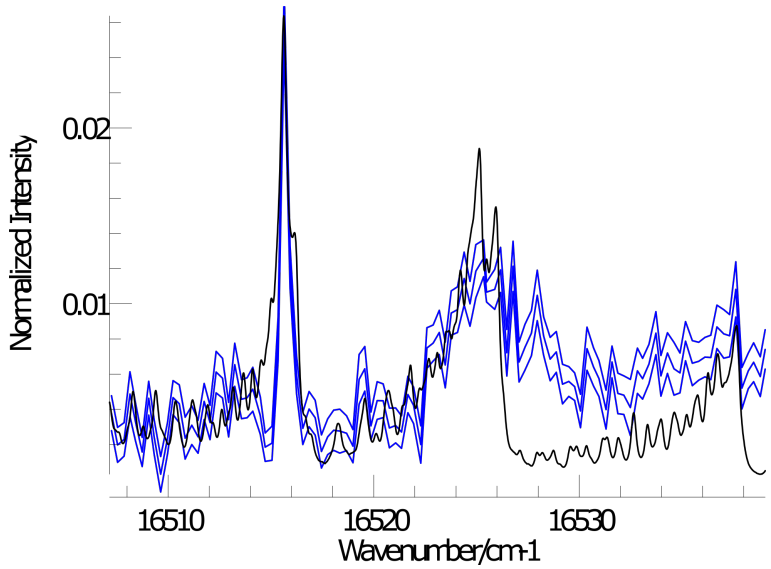

Figure A.9: Rotational-vibrational spectrum of the I $^2\Delta_{5/2} \leftarrow$ A $^2\Pi_{1/2}$ transition.

A.3 Higher vibrational states

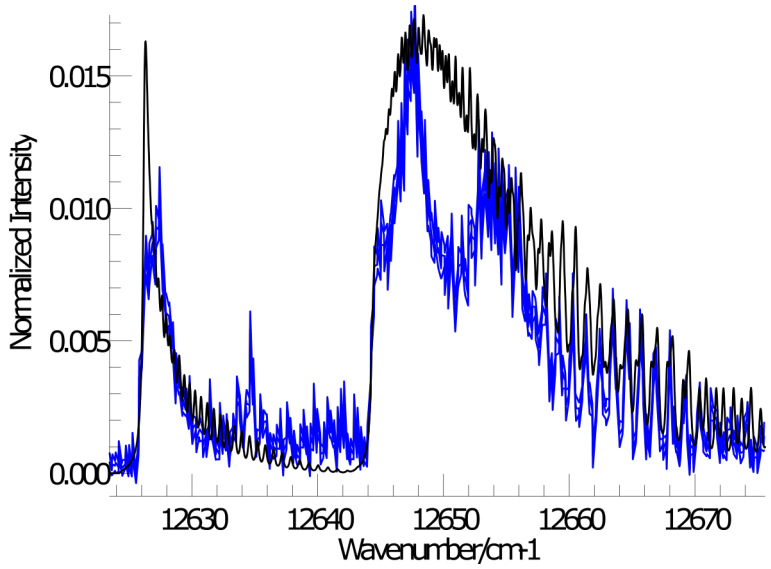

Figure A.10: Rotational-vibrational spectrum of the proposed $E^2\Sigma_{1/2}(\nu = 1)$ vibrational state.

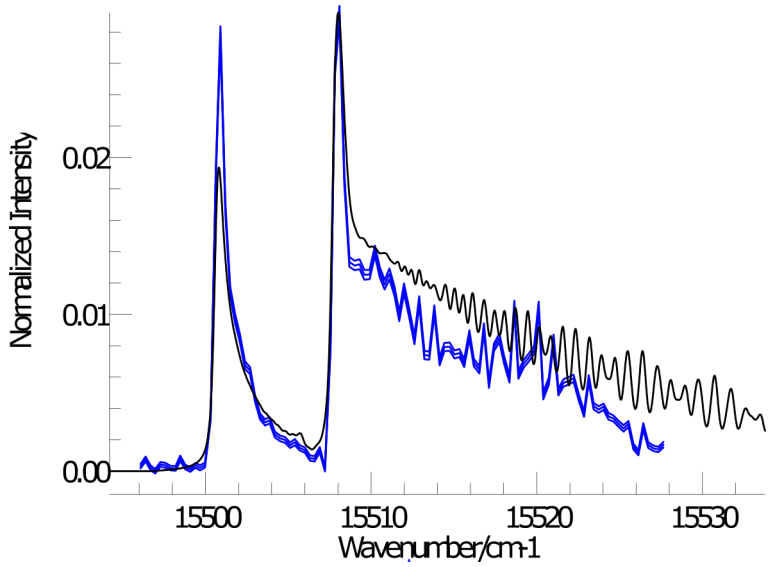

Figure A.11: Rotational-vibrational spectrum of the proposed $F^2\Sigma_{1/2}(\nu \geq 1)$ vibrational state.

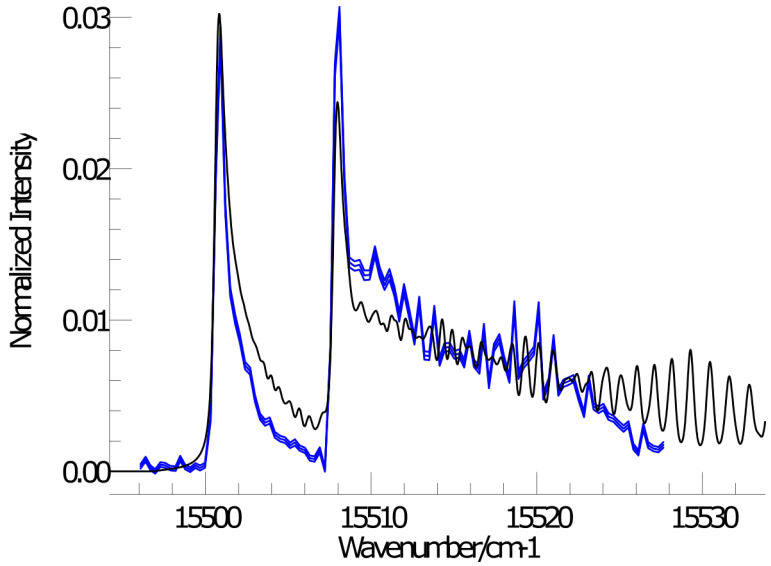

Figure A.12: Rotational-vibrational spectrum of the proposed $G^2\Pi_{1/2}(\nu = 1)$ vibrational state.

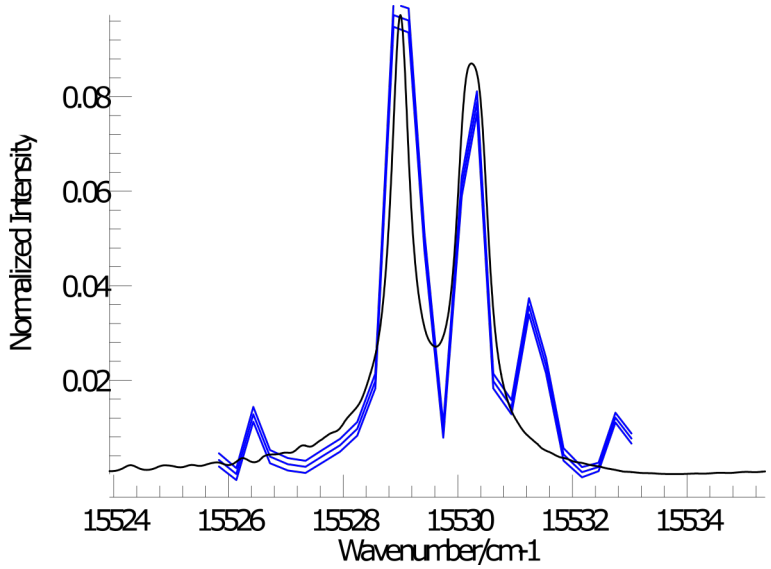

Figure A.13: Rotational-vibrational spectrum of the proposed $G^2\Pi_{1/2}(\nu = 2)$ vibrational state.

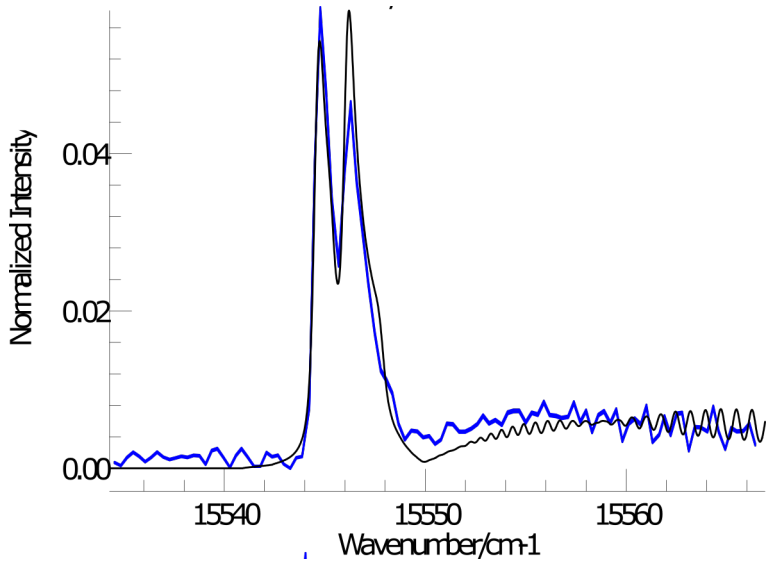

Figure A.14: Rotational-vibrational spectrum of the proposed $G^2\Pi_{1/2}(\nu = 3)$ vibrational state.

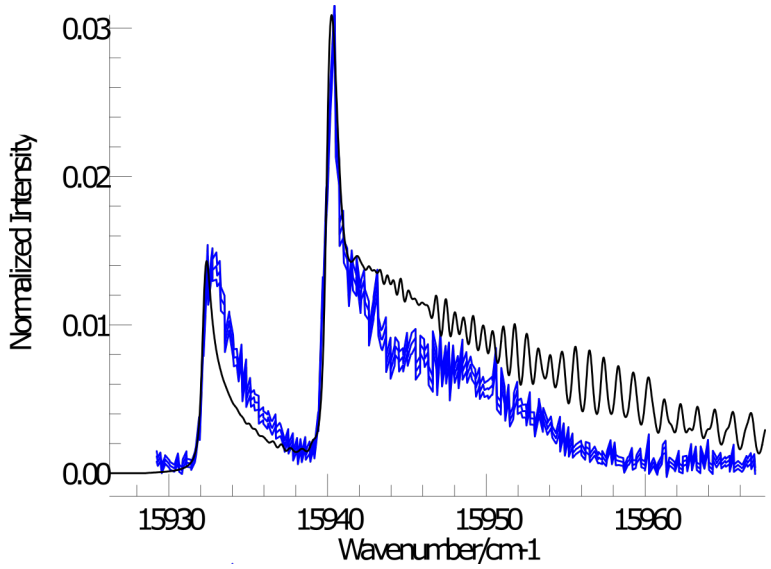

Figure A.15: Rotational-vibrational spectrum of the proposed $G^2\Pi_{3/2}$ (29225.9 cm^{-1}) vibrational state.

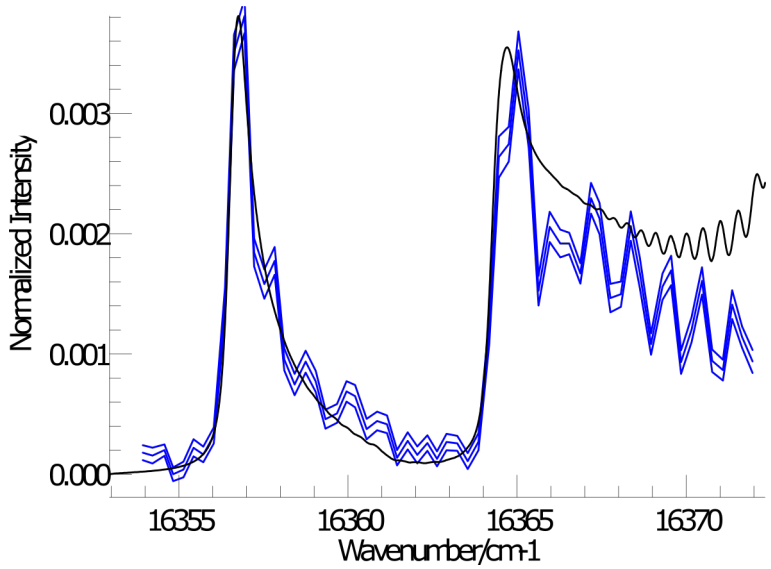

Figure A.16: Rotational-vibrational spectrum of the proposed $H^2\Sigma_{1/2}$ (29650.4 cm^{-1}) vibrational state.

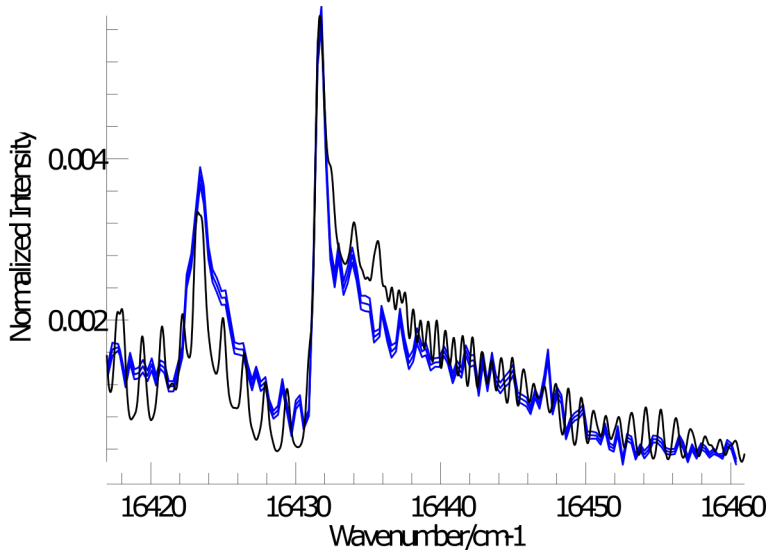

Figure A.17: Rotational-vibrational spectrum of the proposed $H^2\Sigma_{1/2}(\nu = 2)$ vibrational state.

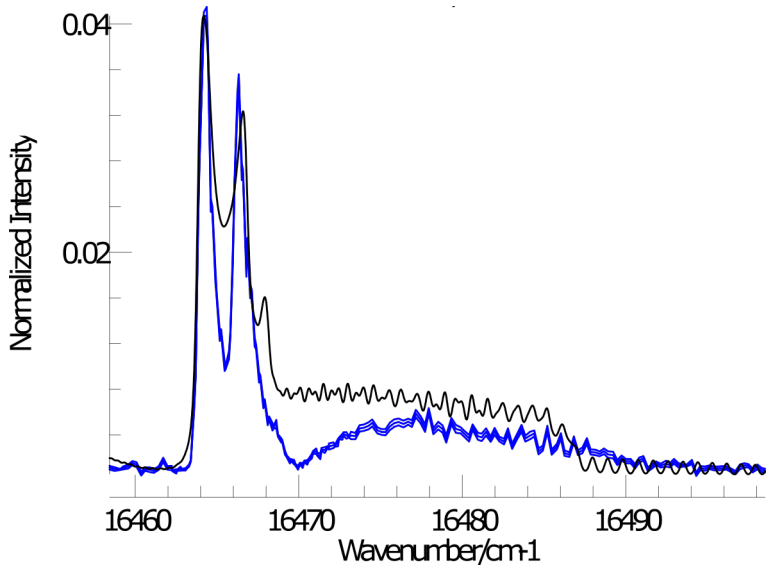

Figure A.18: Rotational-vibrational spectrum of the proposed $G^2\Pi_{3/2}(\nu = 2)$ vibrational state.

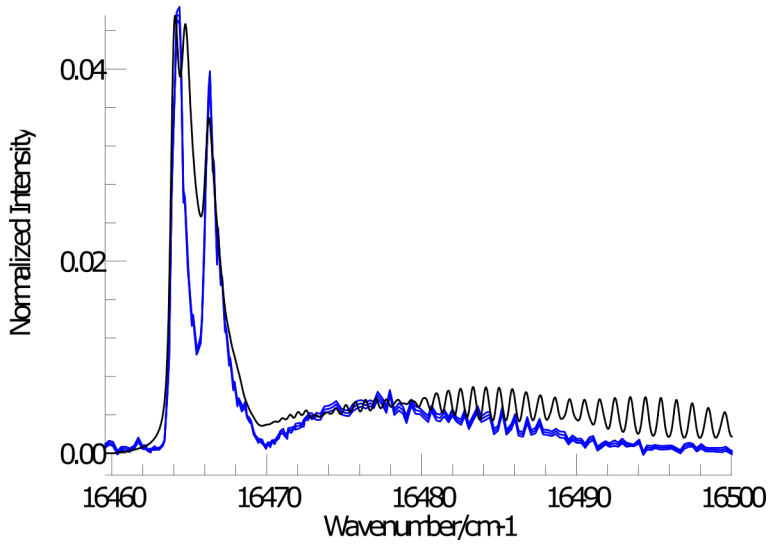

Figure A.19: Rotational-vibrational spectrum of the proposed $H^2\Sigma_{1/2}(\nu = 3)$ vibrational state.

AFDELING
Straat nr bus 0000
3000 LEUVEN, BELGIË
tel. + 32 16 00 00 00
fax + 32 16 00 00 00
www.kuleuven.be